



HAL
open science

Shape Modeling of Dimorphos for the Double Asteroid Redirection Test (DART)

R Terik Daly, Carolyn M Ernst, Olivier S Barnouin, Robert W Gaskell, Eric E Palmer, Hari Nair, Ray C Espiritu, Sarah Hasnain, Dany Waller, Angela M Stickle, et al.

► **To cite this version:**

R Terik Daly, Carolyn M Ernst, Olivier S Barnouin, Robert W Gaskell, Eric E Palmer, et al.. Shape Modeling of Dimorphos for the Double Asteroid Redirection Test (DART). *The Planetary Science Journal*, 2022, 3, 10.3847/psj/ac7523 . hal-03835344

HAL Id: hal-03835344

<https://hal.science/hal-03835344>

Submitted on 31 Oct 2022

HAL is a multi-disciplinary open access archive for the deposit and dissemination of scientific research documents, whether they are published or not. The documents may come from teaching and research institutions in France or abroad, or from public or private research centers.

L'archive ouverte pluridisciplinaire **HAL**, est destinée au dépôt et à la diffusion de documents scientifiques de niveau recherche, publiés ou non, émanant des établissements d'enseignement et de recherche français ou étrangers, des laboratoires publics ou privés.



Shape Modeling of Dimorphos for the Double Asteroid Redirection Test (DART)

R. Terik Daly¹, Carolyn M. Ernst¹, Olivier S. Barnouin¹, Robert W. Gaskell², Eric E. Palmer², Hari Nair¹, Ray C. Espiritu¹, Sarah Hasnain¹, Dany Waller¹, Angela M. Stickle¹, Michael C. Nolan³, Josep M. Trigo-Rodríguez⁴, Elisabetta Dotto⁵, Alice Lucchetti⁶, Maurizio Pajola⁷, Simone Ieva⁶, and Patrick Michel⁸

¹ Johns Hopkins University Applied Physics Laboratory, Laurel MD, USA; Terik.Daly@jhuapl.edu

² Planetary Science Institute, Tucson, AZ, USA

³ University of Arizona, Tucson, AZ, USA

⁴ Institute of Space Sciences (CSIC-IEEC), Barcelona, Catalonia, Spain

⁵ INAF Osservatorio Astronomico di Roma, Via Frascati 33, 00078, Monte Porzio Catone, Roma, Italy

⁶ INAF Astronomical Observatory of Padova, Padova, Italy

⁷ OAPD Astronomical Observatory of Padova, Italy

⁸ Université Côte d'Azur, Observatoire de la Côte d'Azur, CNRS, Laboratoire Lagrange, Nice, France

Received 2022 March 2; revised 2022 May 27; accepted 2022 May 30; published 2022 September 8

Abstract

The Double Asteroid Redirection Test (DART) is the first planetary defense test mission. It will demonstrate the kinetic impactor technique by intentionally colliding the DART spacecraft with the near-Earth asteroid Dimorphos. The main DART spacecraft is accompanied by the Italian Space Agency Light Italian CubeSat for Imaging of Asteroids (LICIACube). Shape modeling efforts will estimate the volume of Dimorphos and constrain the nature of the impact site. The DART mission uses stereophotoclinometry (SPC) as its primary shape modeling technique. DART is essentially a worst-case scenario for any image-based shape modeling approach because images taken by the camera on board the DART spacecraft, called the Didymos Reconnaissance and Asteroid Camera for Optical navigation (DRACO), possess little stereo and no lighting variation; they simply zoom in on the asteroid. LICIACube images add some stereo, but the images are substantially lower in resolution than the DRACO images. Despite the far-from-optimal imaging conditions, our tests indicate that we can identify the impact site to an accuracy and precision better than 10% the size of the spacecraft core, estimate the volume of Dimorphos to better than 25%, and measure tilts at the impact site over the scale of the spacecraft with an accuracy better than 7°. In short, we will know with excellent accuracy where the DART spacecraft hit, with reasonable knowledge of local tilt, and determine the volume well enough that uncertainties in the density of Dimorphos will be comparable to or dominate the uncertainty in the estimated mass. The tests reported here demonstrate that SPC is a robust technique for shape modeling, even with suboptimal images.

Unified Astronomy Thesaurus concepts: Asteroids (72); Near-Earth objects (1092); Asteroid satellites (2207); Impact phenomena (779); Planetary science (1255)

1. Introduction

NASA's Double Asteroid Redirection Test, or DART, is the world's first full-scale planetary defense test. The mission will autonomously navigate to and intentionally collide with a target asteroid, thereby demonstrating the kinetic impactor technique for deflecting an asteroid (Cheng et al. 2020; Rivkin et al. 2021). The kinetic impactor technique is one of several approaches for deflecting a potentially hazardous asteroid off a collision course with Earth (e.g., Gehrels et al. 1994; Perna et al. 2013).

The DART mission will target the moon of the binary asteroid system (65803) Didymos (volume-equivalent diameter, $D = 780$ m). The moonlet, Dimorphos ($D = 171 \pm 11$ m; Scheirich & Pravec 2022), orbits Didymos at a distance of ~ 1.2 km with an orbital period of 11.9216289 ± 0.0000028 hr (Naidu et al. 2021). The detailed physical and dynamical characteristics of the Didymos system have been described elsewhere (e.g., Pravec et al. 2006, 2012, 2016; Fang & Margot 2012; Cheng et al. 2016; Michel et al. 2016; Naidu et al. 2020; Rivkin et al. 2021; Scheirich & Pravec 2022). The DART spacecraft launched on

2021 November 24 at 1:21 a.m. EST and will impact Dimorphos at 6.15 km s^{-1} at 23:14 UTC on 2022 September 26. The DART spacecraft will deploy the Italian Space Agency Light Italian CubeSat for Imaging of Asteroids (LICIACube; Dotto et al. 2021) approximately 10 days before impact so that LICIACube may witness the event.

The DART mission will estimate the momentum transfer enhancement parameter, β , imparted to Dimorphos by the DART spacecraft. This parameter is key to understanding how well DART performed as a kinetic impactor and for planning future mitigation missions, should the need arise (Rivkin et al. 2021). In order to determine β , the pre-impact momentum of Dimorphos must be compared to its post-impact momentum, taking into account the momentum imparted by the DART spacecraft. Additional momentum carried away by the debris (ejecta) excavated from the impact must also be accounted for (e.g., Holsapple & Housen 2012; Jutzi & Michel 2014; Scheeres et al. 2015; Tanbakouei et al. 2019). Obtaining a measure of β requires a measure of the mass of Dimorphos. Estimating β also requires information about the impact site (Pajola et al. 2022, this focus issue) because the character of the impact site will affect the amount and velocity of the ejecta (Stickle et al. 2022, this focus issue). Furthermore, the shapes of the two bodies affect the mutual dynamics, contributing to β (Richardson et al. 2022).



Original content from this work may be used under the terms of the [Creative Commons Attribution 4.0 licence](https://creativecommons.org/licenses/by/4.0/). Any further distribution of this work must maintain attribution to the author(s) and the title of the work, journal citation and DOI.

Table 1
Summary of Parameters of Interest to the DART Investigation that Will Be Derived from the Shape Model of Dimorphos

Parameter	Use	Desired Uncertainty and Rationale ^a
Volume of Dimorphos	Used in conjunction with an estimated density to determine the mass of Dimorphos, which feeds into the β measurement.	<25%. This level of uncertainty in volume is comparable to or less than the 25% uncertainty assumed in asteroid density.
Impact site location	Used as an input into numerical models of the DART impact.	<2.5 m. The core of the DART spacecraft has a maximum envelope of 2.5 m, so this uncertainty means that the impact site would be identified with an accuracy comparable to the size of the spacecraft core.
Surface tilts at impact site	Used to determine surface normal, which will be used as an input to numerical models of the DART impact.	<15°. Unless the impact angle is <45°, uncertainties of 15° should not affect interpretation of the impact.

Note.

^a The DART project carries no requirements for the accuracy of these quantities. They are determined on a best-effort basis.

DART will determine the mass of Dimorphos based on the volume of a global shape model and an assumed density. Hence, shape modeling efforts are a pivotal part of the DART mission. If we assume a 25% uncertainty on the estimated density and that the shape model was perfect, the resulting uncertainty in β would also be 25%. Therefore, 25% represents the smallest possible uncertainty for our β measurement, given the assumed density uncertainty. Later, the Hera mission (scheduled to be launched in 2024 October by the European Space Agency, ESA) will measure the mass of Dimorphos to better than 10% during its rendezvous with the Didymos system in 2027. Hera will further refine the value of β , analyze in detail the properties and internal structure of Dimorphos, as well as assess the size and morphology of the crater left by DART (Michel et al. 2022).

The DART investigation will rely on images taken by the spacecraft as it approaches Dimorphos to identify and characterize the impact site. Impact simulations (e.g., Syal et al. 2016; Feldhacker et al. 2017; Raducan et al. 2022) show that the momentum ultimately carried by the ejecta is a complicated function of impact angle and surface geology. Experiments also attest to the importance of initial coupling on ejecta in coarse-grained targets (Barnouin et al. 2019). Blocks or boulders near the impact site most strongly affect the outcome of the DART impact if the boulders are comparable in size to the core of the DART spacecraft (Stickle et al. 2022, this focus issue). The core of the DART spacecraft has a maximum envelope of 2.5 m. Hence, it would be ideal to know the impact site with an accuracy better than 2.5 m. See Section 5.6 for additional details.

Impact angle affects the character of the ejecta curtain (Gault & Wedekind 1978; Anderson et al. 2003) and the direction of the momentum vector (Syal et al. 2016; Stickle et al. 2022, this focus issue). Hence, the DART project needs to know the surface normal at the impact site, averaged over a region that is the size of the spacecraft. The impact angle of the DART spacecraft can be determined by deriving the surface normal of the shape model at the location of the DART impact relative to the trajectory of the incoming spacecraft. The surface normal depends on the tilt of facets in the shape model. Hence, it is important to understand expected uncertainties in the tilt of the shape model facets at the impact site. Based on numerical models and experiments, we expect that surface tilts meaningfully perturb ejecta and momentum transfer only for an oblique impact below 45° (Stickle et al. 2022, this focus issue).

Here, we review the images that the DART spacecraft and LICIAcube will acquire, describe the process for building a global shape model of Dimorphos and a local digital terrain

model (DTM) of the impact site (hereafter referred to as the impact site DTM), and discuss the tests performed to assess the expected quality of the models. Table 1 summarizes the parameters that will be derived from the shape model of Dimorphos and used by the DART project. The work presented focuses on the use and testing of stereophotoclinometry (SPC; Gaskell et al. 2008; Al Asad et al. 2021; Palmer et al. 2022; Weirich et al. 2022) as a shape modeling technique. We also plan to use a complementary approach based on photogrammetry (Thomas et al. 2017; Re et al. 2022) to build a comparison impact site DTM. This 3D reconstruction software for planetary surfaces (Simioni et al. 2021) will complement the SPC efforts, but is not discussed further here. We provide estimates of the expected performance of the SPC-derived global shape model and impact site DTM.

2. DART Observations of Dimorphos

The DART mission will acquire two data sets that can be used to model the shape of Dimorphos and to determine the location and character of the DART impact site. The highest-resolution images of Dimorphos will come from the Didymos Reconnaissance and Asteroid Camera for Optical navigation (DRACO; Fletcher et al. 2018) on board the DART spacecraft. This instrument, derived from the Long Range Reconnaissance Imager (LORRI) on New Horizons (Cheng et al. 2008), is a narrow-angle telescope with an instantaneous field of view (IFOV) of 4.96 μ rad (in a 2 × 2 binned pixel), a 208 mm aperture, $f/12.6$, and a 0.29° field of view (FOV). DRACO has a complementary metal-oxide semiconductor (CMOS) detector and will stream panchromatic (400–1000 nm), 512 × 512 pixel images back to Earth in real time in the hours and minutes before impact.

The highest-resolution image required to be returned by DART has a 66 cm pixel scale (Figure 1). This image will be acquired approximately 20 s before impact. At this scale, Dimorphos only covers a fraction of the 512 × 512 pixel image and will be approximately 250 pixels across in the long dimension. It is expected that DART will be able to return images until 2–3 s before impact; the final image will have a pixel scale <10 cm (Figure 1). The asteroid will fill the DRACO FOV only during the last ~10 to 15 s before impact. The exact time when Dimorphos fills the FOV depends on the asteroid size, shape, and position in the image. While the spatial resolution of DRACO images is very high, they all have near-identical geometries at a constant phase angle of ~60°. Resolved DRACO images will provide little to no stereo-parallax data. Effectively, each image is a higher-resolution

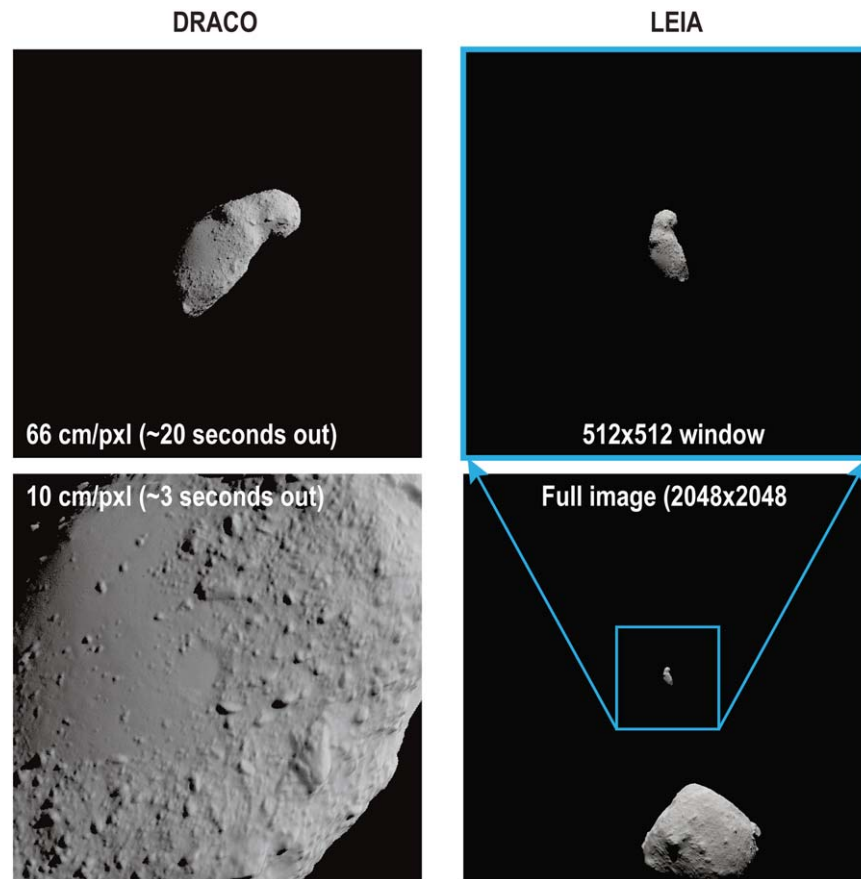


Figure 1. Simulated DRACO and LEIA images. A scaled-down version of Itokawa is a stand-in for Dimorphos, while a scaled-down Ryugu stands in for Didymos. DRACO images (left column) progressively zoom in on the impact site. The highest-resolution LEIA image (right column) is much coarser than the expected DRACO images, which limits the amount of detail that can be seen in the LEIA image. However, LEIA provides alternative viewing geometries and additional limb information that benefit the long-wavelength shape. The LEIA images are 2048×2048 vs. DRACO’s 512×512 images in Terminal. The upper-right panel shows a 512×512 window of the LEIA image below. Comparing the two simulated DRACO images against the upper-right panel gives a good sense for what the finest-spatial-scale LEIA images will look like vs. the required and expected DRACO images.

version of the one before it. Even with multiple DRACO images, we are effectively building a shape model from a single view.

The LICIACube spacecraft (Dotto et al. 2021) carries two cameras: the LICIACube Explorer Imaging for Asteroid (LEIA), which is a 2048×2048 pixel, panchromatic camera with an IFOV of $25 \mu\text{rad}$, and the LICIACube Unit Key Explorer (LUKE), which is a 2048×1048 pixel, wide-angle, three-band color imager (RGB Bayer pattern filter) with an IFOV of $78 \mu\text{rad}$. For shape modeling purposes, we will use only the higher-resolution LEIA images. At closest approach, which occurs 165 s after impact, LEIA will image Dimorphos’ surface with a spatial scale close to 1.4 m px^{-1} (Figure 1). Ejecta may be visible in the images. The long axis of Dimorphos will only be about ~ 115 pixels across in the highest-resolution LEIA image. LICIACube will attempt to image the impact site and much of the illuminated portions of Dimorphos at a range of phase angles that rapidly changes from 58° to 110° (Pajola et al. 2022, this focus issue). Only a subset of the LICIACube images from a narrower range of phase angles will resolve Dimorphos well enough to contribute to shape modeling efforts. However, the presence of ejecta in the post-impact images may limit the usefulness of the images for shape modeling.

DRACO data are streamed directly to Earth in the hours leading up to impact, whereas it may take several weeks after

impact to downlink the full LICIACube data set. Therefore, the shape modeling efforts will initially only use DRACO images. The subset of LICIACube images suitable for shape modeling will be incorporated into the shape model as they become available.

3. Digital Terrain Model Development for DART

Stereophotoclinometry (SPC) is the baseline technique employed to model the shape and topography of Dimorphos. SPC was first developed in the mid-1980s to model the surface of Io (Gaskell et al. 1988). SPC generates a DTM by combining geometric stereo techniques (e.g., Wolf & Dewitt 2000) with photoclinometry. It uses both shading and lighting direction. SPC also estimates the spacecraft position and attitude, and, in some instances, pole orientation and spin rate (Gaskell et al. 2008; Barnouin et al. 2020). SPC has been used to model a broad suite of objects ranging in size from (25143) Itokawa (Gaskell et al. 2008) to Mercury (Perry et al. 2015), including, but not limited to, (433) Eros (Gaskell et al. 2008), 67P/Churyumov–Gerasimenko (Jorda et al. 2016), (101955) Bennu (Barnouin et al. 2019), (162173) Ryugu (Watanabe et al. 2019), the Martian moons Phobos and Deimos (Ernst et al. 2018), and 9P/Tempel (Ernst et al. 2019). SPC has been used during spacecraft operations to aid navigation at Itokawa (Gaskell et al. 2008), (4) Vesta (Gaskell 2012), and the dwarf planet (1)

Ceres (Park et al. 2019). It was critical for navigation at Bennu (e.g., Palmer et al. 2022; Weirich et al. 2022) and helped to ensure a safe sampling of the surface (Mario et al. 2022; Olds et al. 2022).

SPC was chosen for DART because it has been used successfully to model irregularly shaped bodies from single flybys (e.g., (21) Lutetia, Sierks et al. 2011; (2867) Steins, Jorda et al. 2012). In general, images from a single flyby often overlap, with very rapid changes in stereo parallax (e.g., Magrin et al. 2012), and just one illumination condition from which shape can be captured from surface shading. SPC successfully builds DTMs for such flybys because it uses all the shading information within images at the pixel level and uses as much stereo information as is available. SPC also makes use of all images at its disposal, regardless of resolution and phase angle. Lower-resolution images lead to an initial, lower-resolution shape model that provides a framework for incorporating higher-resolution images to make higher-resolution global and local shape models. SPC also makes use of limb observations to complement its shading and stereo data constraints. Limbs are typically observed during flybys and often provide the only constraints on parts of the shape model.

DART will focus on modeling the shape of Dimorphos. As time permits, however, the DART team will also generate an SPC shape model of Didymos using DRACO and any available LICIAcube images. LICIAcube images of Didymos will likely be less affected by ejecta than LICIAcube images of Dimorphos. The resolution of the images of Didymos are, at best, a few meters per pixel and are again limited to the imaged, illuminated portions of the asteroid, which comprises one-half of the object. The existing radar model (Naidu et al. 2020) will provide the starting point for the SPC shape model derived from these images.

3.1. Expected Limitations of Stereophotoclinometry for DART

Assessments undertaken for the OSIRIS-REx mission (Barnouin et al. 2020; Al Asad et al. 2021; Palmer et al. 2022; Weirich et al. 2022) demonstrated that the accuracy of SPC shape models ranges between $1\times$ and $2\times$ the resolution of the best images when the input images for a given part of the surface meet the following criteria: (1) at least four different observer elevations and azimuths; (2) varying incidence angles; (3) a fifth image near 0° emission and 10° incidence to aid the relative albedo solution; (4) comparable spatial resolution across the five-image set with one or two images at or below the desired ground sample distance (GSD) of the topographic model and no image exceeding this GSD by more than a factor of 5. When these criteria are met, the formal uncertainty reported by SPC provides a good estimate of the absolute accuracy of a shape model to within $1\text{--}2\times$ this reported uncertainty.

The DART mission cannot provide this optimal set of images of Dimorphos. Rather, the shape modeling of Dimorphos will represent a stressing case for SPC. Indeed, DRACO will acquire images useful to SPC only in the mission's final 2 minutes before impact. During this time, each DRACO image is redundant to the previous one, but at a higher resolution (see Section 2 and Figure 1). Moreover, only about half of Dimorphos will be lit at the time of the DART impact, and neither DRACO nor LEIA will image all of the lit portion of the body. Hence, shape modeling for DART using DRACO images alone is an exercise in how well one can estimate the shape of an

object from images with essentially no stereo in which less than half of the body is both seen by the camera and illuminated. To constrain the shape model in areas that are neither visible nor illuminated, we will use constraints on axial ratios (a/b and b/c) obtained from light curves from the ground (Pravec et al. 2006, 2012, 2016, 2022; Scheirich & Pravec 2022), from earlier, unresolved DRACO images of the Didymos system that will be taken in the days leading up to impact, and from the a/b and b/c axial ratios of secondaries in other binary asteroid systems.

3.2. How Stereophotoclinometry Works

SPC uses a photometric function, along with all the imaging data available, to estimate the surface tilts (angle of surface relative to radial vector) at each pixel in a local DTM, or "maplet," via a linear-estimation solution that minimizes the residual of the summed-square brightness at each maplet pixel. Sensitivity testing (Barnouin et al. 2020; Weirich et al. 2022) has revealed that the choice of photometric function has little effect on the final products, likely because SPC's optimum viewing phase is between 50° and 120° , where most photometric models behave similarly. The tilts are then integrated to heights to produce the surface topographic data within each maplet, usually a 100×100 pixel local DTM. Geometric stereogrammetry is used to define the location of a maplet center. When building a global model, individual maplets are joined together. The mutual connections of the global model are controlled by overlapping maplets, limbs, and stereo, which constrain the tilt-to-height integration between maplets to provide an estimate of the global surface. Linear estimation provides formal uncertainties for the spacecraft state and the shape of the target. In the end, the SPC estimation process can provide solutions for an object's center of figure, pole location, wobble, rotation state, and volume (Gaskell et al. 2006, 2008). Nevertheless, due to the limited imaging conditions, SPC for DART will determine only volume.

3.3. The DART Stereophotoclinometry Process

The overall process to be used by DART for generating shape models of Dimorphos and Didymos (best effort) is outlined in Figure 2. Figure 3 shows the evolution of the shape model through time. Here, we briefly discuss the different stages in the process. For more details on SPC, refer to Gaskell et al. (2008) and Palmer et al. (2022).

Starter shape. The SPC process begins with a starter shape. Currently, we have very little information about the shape of Dimorphos, and the limited information that we do have comes from light-curve observations (Pravec et al. 2022; Scheirich & Pravec 2022). These observations, in concert with observations of the secondaries in other binary systems, help to constrain the axial ratios (a/b and b/c) of Dimorphos. In particular, light-curve axial ratios provide the best information we will have about the shape of Dimorphos until DRACO resolves Dimorphos in the minutes leading up to the DART impact. The current plan is to use a triaxial ellipsoid with light-curve axial ratios as the starting shape model. The DART project has adopted a/b and b/c axial ratios for Dimorphos (Rivkin et al. 2021), and these will serve as a starting point. The ellipsoid will be expanded or shrunken in size to match the extent of Dimorphos in DRACO images (Figure 3(a)). Depending on what the images of Dimorphos look like, we may choose a different starting shape model, as discussed in the conclusion of

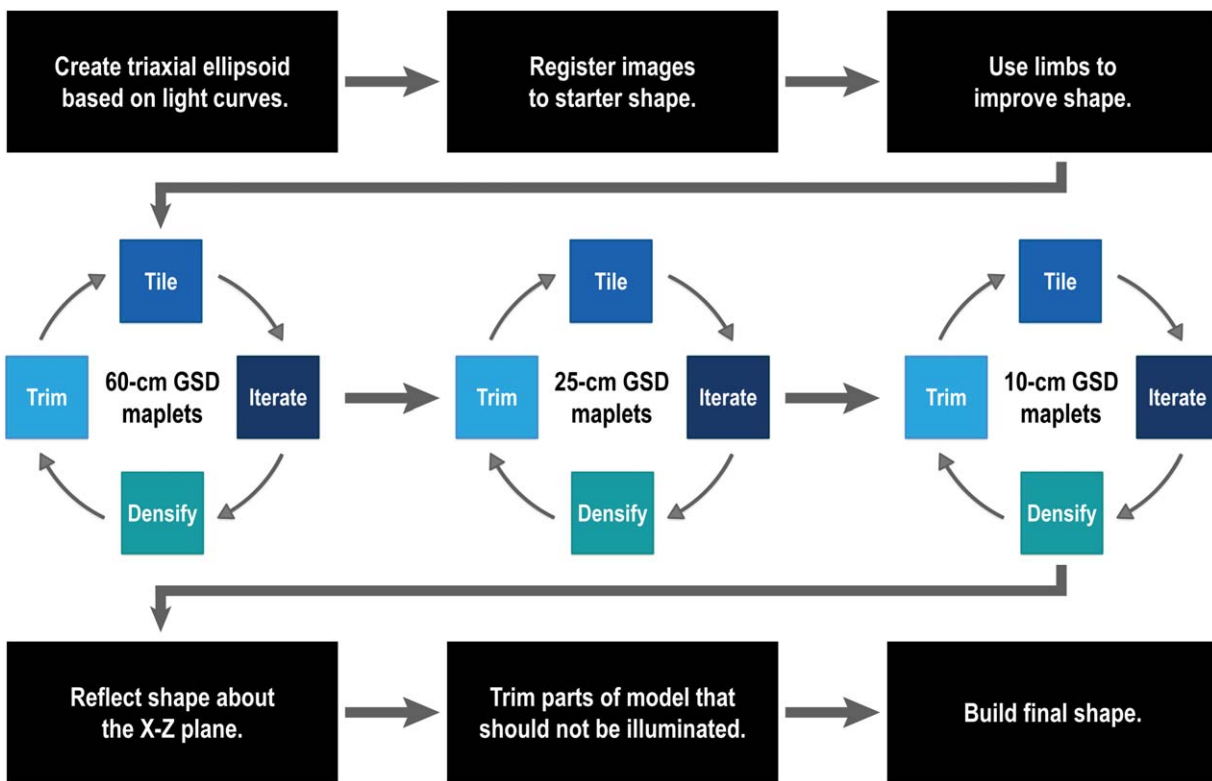


Figure 2. Stages of the shape modeling process used in the DART mission.

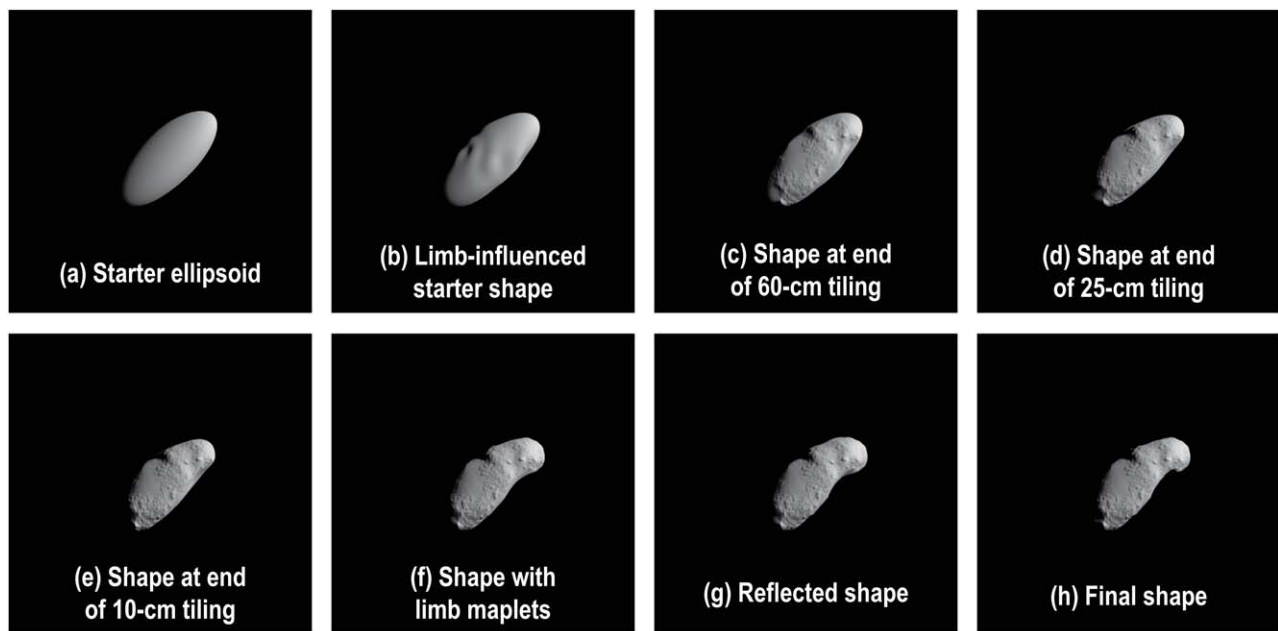


Figure 3. Shape model at various stages of development. Shape model development progresses left to right, top to bottom. In stages (f)–(h), the changes are subtle and primarily occur along the limb. This test is based on simulated images of the scaled-down version of Itokawa.

the paper. But, for now, the baseline plan is to use a triaxial ellipsoid. The SPC starter shape for Didymos will be the radar-derived shape model from Naidu et al. (2020).

Image registration. Dimorphos will move within the DRACO and LEIA images. The images to be used for shape modeling must be registered to one another and to the starter shape before they can be used to build maplets. Registration is done using an SPC program called *register*. See Gaskell et al.

(2008) and Palmer et al. (2022) for additional details about how *register* works in SPC.

Limbs. Limbs are a valuable source of information in our limited image set. The DRACO images all effectively show the same limb, whereas LEIA images can supply a few additional limbs. Constraints from limbs will be used to improve the early shape and better register the images before topographic modeling begins. An SPC program called *limber* identifies

limb points in images. The SPC programs *vecs2cube* use those limb vectors to produce a new shape model that incorporates limb information (e.g., Figure 3(b)).

Topographic modeling. With a limb-improved starter shape and registered images, shape modeling advances into core SPC processing: maplet generation and iterations. Topographic modeling in SPC is performed on a per-maplet basis (see Section 3.2), primarily using an SPC program called *lithos*. First, the visible surface of Dimorphos is tiled with maplets with a relatively coarse GSD of 60 cm. An emission angle cutoff is employed to remove images with a high emission angle (i.e., near the limb), which can degrade the solution. Generally, we use an emission angle cutoff of 60° . As maplets approach the limb, some maplets may accept images with emission angles as high as 70° in an effort to maximize maplet coverage with the limited imaging data. Once the body has been tiled, the entire set of maplets is iterated to improve the topography solution and incorporate information from overlapping maplets. The spacecraft position and camera pointing are updated based on the locations of images in maplets and maplets in images. The maplet set is then iterated additional times to improve the solution. Once the solution converges, overlapping maplets are averaged to create a new global shape model using an SPC program called *densify*. Areas not covered by maplets remain unchanged. The model is then trimmed to remove regions that are not visible and lit in the input images (see “trimming,” below, for additional information).

This cycle is then repeated at progressively finer maplet GSDs as indicated in Figures 3(c)–(e). We will use three increasingly fine scales of maplets for modeling Dimorphos, with GSDs of 60, 25, and 10 cm. The finer-scale maplets also include a set of limb-only maplets. Limb-only maplets are placed along the image limb and use only the shape and limb points to condition the tilt-to-height integration. Limb maplets are not necessary when global imaging coverage exists, but in the case of DART, where so little of the body is seen, limb-only maplets continue to provide essential constraints on the bulk shape and improve the agreement between the images and the shape (Figure 3(f)). Depending on the resolution of the final DRACO image, an even finer set of standard maplets may be added at and around the impact site. Due to the limited nature of the resolved images collected both from DART and LICIAcube (a very narrow phase angle range, collected at essentially one moment in time), SPC will not be used to update the pole or rotation state of Dimorphos. That information will be collected from earlier DRACO data of the system and ground- and space-based telescopic observations.

Reflection. Since we will have good information about the side of the asteroid seen by DRACO and no information about the unseen side, we will reflect a very-low-resolution version of the shape model about the X - Z plane, replacing the unseen portions with a low-resolution shape (Figure 3(g)). That back side of the shape model will remain at a very low resolution, however, since we do not have any detailed information about its topography.

Trimming. The model is trimmed at several stages in the SPC modeling process to remove areas that are neither visible nor lit in the images. This step takes advantage of the fact that we know where the camera did *not* see the body, so the model must also not be seen in those regions. Trimming is done using an SPC program called *trimmer*. Because the reflection in the

previous stage will have changed significantly the shape on the back side, areas that were previously trimmed sufficiently may now be illuminated. We trim the model one final time to better match the images.

Final shape. The final shape (Figure 3(h)) is built using a coarse version of the reflected, trimmed model as a starting point. Areas covered in maplets will be modeled from that topography, with areas covered by multiple maplets being defined as the average of those overlapping maplets, weighted by the spatial resolution of the maplets (Gaskell et al. 2008; Palmer et al. 2022). Limb points also contribute to the final shape. The final global shape model will have ~ 3 million facets, but topographic detail will exist only in the areas covered by standard maplets.

3.4. Shape Modeling Products

DART will produce a global shape model of Dimorphos and an impact site DTM, accompanied by ancillary data products. A shape model of Didymos will be produced on a best-effort basis. The shape modeling efforts will also provide improved estimates of the spacecraft trajectory and pointing relative to Dimorphos and precisely identify the impact site. These models will be delivered to the Planetary Data System (PDS) as part of the DART collection. The shape models and coregistered images will also be available in the Small Body Mapping Tool (SBMT; Ernst et al. 2018). The SBMT is a 3D visualization and geospatial analysis tool for small bodies. In the SBMT, users will be able to visualize uncertainties in the shape models as basemaps so that people know whether the models can be trusted and where they are poorly constrained.

The resulting global shape models and impact site DTM will be used to generate derived geophysical products, including maps of elevation (height relative to a geoid, assuming a constant density), slope, roughness, and surface tilt with respect to the spacecraft impact vector. These products are similar to derived products generated for shape models by the OSIRIS-REx mission, as described in detail in Barnouin et al. (2020). Such derived products are critical for understanding the nature of the impact site and the direction of the momentum vector produced by the DART impact, the geological nature and evolution of Dimorphos (Pajola et al. 2022, this focus issue), as well as the pre- and post-impact dynamic evolution (Richardson et al. 2022). Similar products will be generated for the global shape model of Didymos.

4. Shape Modeling Testing

We performed a series of tests to assess how well DART will be able to determine the impact site, estimate the volume of Dimorphos, and characterize surface tilts at the impact site, given the very limited images that will be available from DRACO and LEIA. These tests explored our sensitivity to the shape of the body, the effect of uncertainties in spacecraft trajectory and pointing, and the incorporation of LEIA images. Table 2 lists the names and parameters for each test discussed in this paper.

For each test, we generated simulated DRACO and LEIA images of Dimorphos using a truth shape model and a set of realistic spacecraft trajectories (see below). We then used the shape modeling process described in Section 3.3 to build the shape model, and we assessed the reconstructed shape model in terms of impact site location, volume, and surface tilts. These

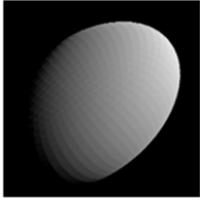
Name	Extent, X-axis (km)	Extent, Y-axis (km)	Extent, Z-axis (km)	Volume (km ³)	Simulated DRACO Image Example
Ellipsoid	0.208	0.160	0.133	0.00231	
Shrunken Itokawa	0.141	0.105	0.093	0.000276	
Shrunken Bennu	0.189	0.182	0.167	0.00231	

Figure 4. Truth shape models used to simulate images.

Table 2
Shape Modeling Tests Undertaken for DART

Test	Target Shape	DRACO	LEIA	Attitude & Trajectory Errors
Ellipsoid	Ellipsoid	Yes	No	No
Itokawa_DRACO	Shrunken Itokawa	Yes	No	No
Itokawa_DRACO+LEIA	Shrunken Itokawa	Yes	Yes	No
Bennu_ideal	Shrunken Bennu	Yes	No	No
Bennu_errors	Shrunken Bennu	Yes	No	Yes

differences between the truth and reconstructed models allow us to provide reasonable estimates of the uncertainties associated with the impact site, volume, and tilt measurements made after the DART impact, when there is no truth model to compare against.

4.1. Truth Shape Models

The detailed shape of Dimorphos will not be known until just a few minutes before impact. For this reason, we decided to use three different truth shape models as stand-ins for Dimorphos in order to see how sensitive the shape modeling process is to the true shape of Dimorphos (Figure 4). The first model was a simple triaxial ellipsoid. Its aspect ratios were set by the Dimorphos design reference asteroid (DRA; Rivkin et al. 2021). The second and third models were based on existing models of Itokawa (Gaskell et al. 2008) and Bennu (Daly et al. 2020). The Itokawa and Bennu models were shrunk to approximately match the extent (for Itokawa) and the best-available volume estimate (for Bennu) of Dimorphos. An appropriately scaled Ryugu shape model (Watanabe et al. 2019) served as a stand-in for Didymos. The +X-axes of the shrunken Itokawa and Bennu shape models pointed at

Didymos. The +Z-axes of the shrunken Itokawa and shrunken Bennu shape models were parallel with the +Z-axis of Didymos.

Figure 5 shows each of these three shape models along their principal axes. The triaxial ellipsoid was used for the ellipsoid test. This test was included as a simple case to see whether we could reproduce a triaxial ellipsoid using our shape modeling process. If we could not match the extent of the triaxial ellipsoid in the images, we would have little confidence that we could reasonably reproduce a more complicated shape. Shrunken Itokawa was used for the Itokawa_DRACO and Itokawa_DRACO+LEIA tests. Shrunken Bennu was used for the Bennu_ideal and Bennu_errors tests. The ellipsoid was chosen as the simplest test case. The Itokawa model was chosen to explore the effect of a bilobate, elongated asteroid on our shape modeling performance. The Bennu model provided an example of a more axisymmetric and uniform shape, but with a diamond-shaped profile.

The simulated images did not include variations in surface albedo. While C-type asteroids Bennu and Ryugu have both shown significant surface albedo variations across their surface, sometimes varying locally by 50% (DellaGiustina et al. 2020;

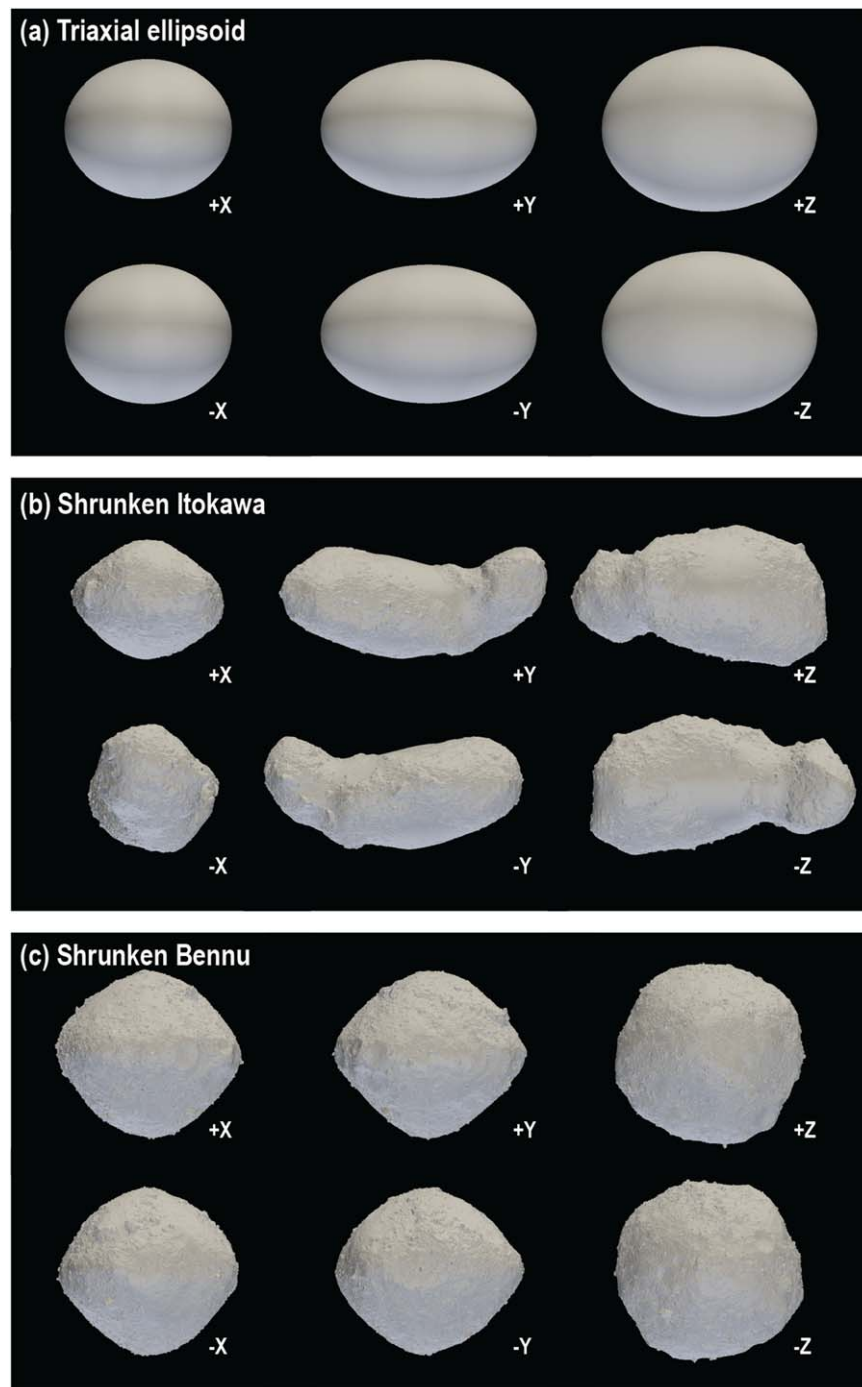


Figure 5. Six views of the truth shape models used for shape models tests. Three truth models were used: (a) a triaxial ellipsoid, (b) a shrunken Itokawa, and (c) a shrunken Bennu. The view is sized to best fit each model; the models themselves are different sizes.

Tatsumi et al. 2021), this level of variation has not been seen on S-type asteroids such as Itokawa (Kitazato et al. 2008) or Eros (Murchie et al. 2002), which show at most 20% variation in albedo limited over small portions ($<1\%$) of their total surface area. Didymos and Dimorphos are both S-types (de León et al. 2006, 2010; Ieva et al. 2022). Most apparent surface brightness variations seen in images of Eros and Itokawa are related to variations in surface tilt, which we account for in our renderings by using the modified Lommel–Seliger photometric model (McEwen 1996). This photometric model ensures that smaller emission (i.e., angle subtended between an observer and the surface normal) and incidence (i.e., angle subtended

between the Sun and the surface normal) angles lead to brighter surfaces.

4.2. Spacecraft Trajectory and Pointing

To simulate the images, we used a spacecraft trajectory modified from what was produced by the DART project in mid-2020, a year or so before the actual launch date was known. These simulations also used an earlier ephemeris of Dimorphos around the barycenter of the Didymos system. This trajectory led to an impact into Dimorphos on 2022 October 1, at 10:29:07 UTC. The baseline trajectory had no

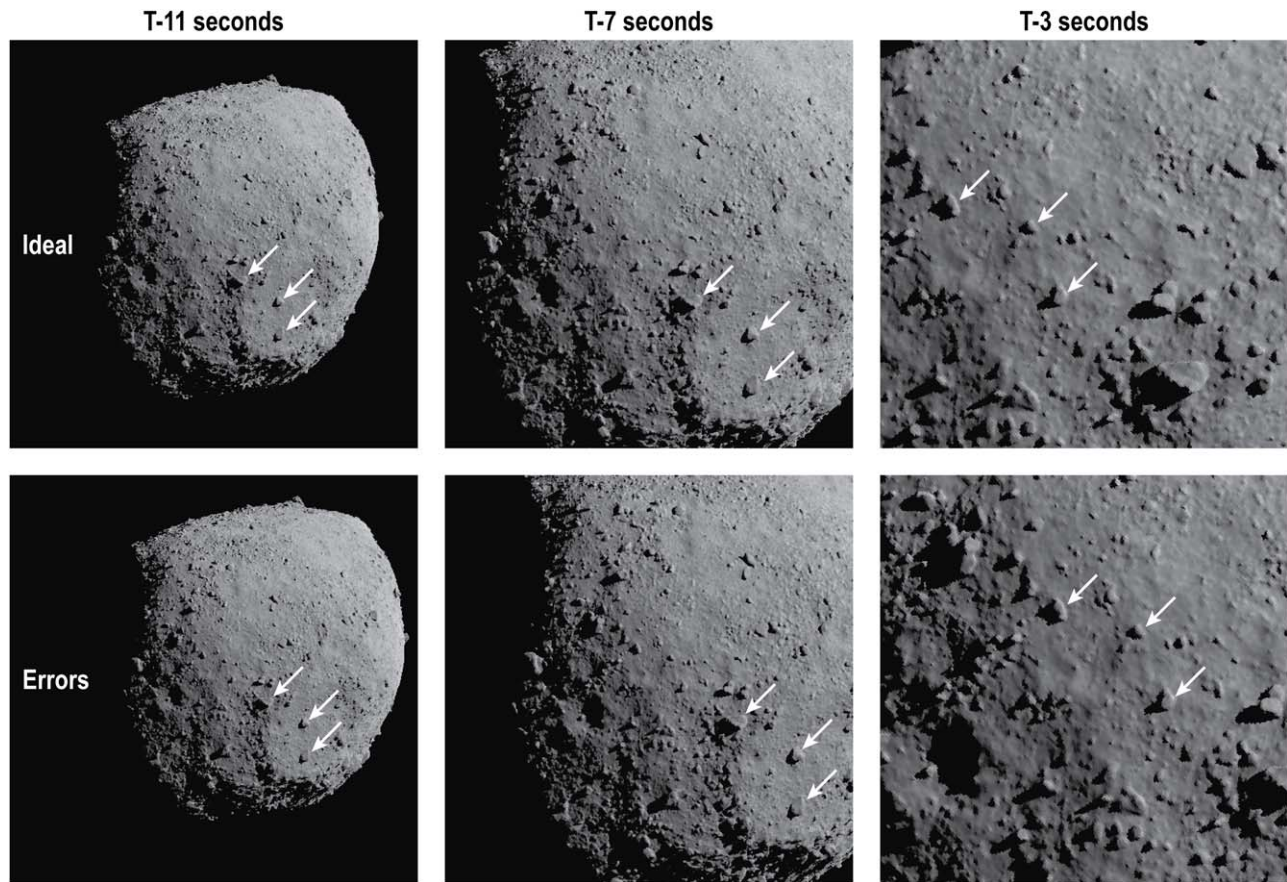


Figure 6. Differences in simulated DRACO images in the ideal and error Bennu cases. In the ideal case, there are no spacecraft uncertainties in the trajectory and the body is always centered in the image. In the error case, there is a ~ 15 m spacecraft uncertainty and 0.1 mrad pointing uncertainty. In the error case, the body moves around in the camera frame, and the impact point is different than in the ideal case. Compare, for example, the positions of indicated features, as well as the location of the limb and terminator relative to the edges of the images, in the top (ideal) and bottom (error) rows. The times listed are the number of seconds before impact. The offsets are clearest in the T-3 seconds image. The impact sites are located at the center of the T-3 seconds image, in each respective case.

uncertainties, with the DART spacecraft striking Dimorphos at $-29.12^\circ\text{N } 90.01^\circ\text{E}$ at $\sim 7.2\text{ km s}^{-1}$. The simulated LICIAcube trajectory employed flew by the system at ~ 50 km several tens of seconds after impact. All the images used for our analysis were developed using this baseline trajectory, and the aforementioned ephemeris of Dimorphos around the system’s barycenter, regardless of truth shape model. We also produced attitude files that described the pointing of the spacecraft during the acquisition of the simulated images. The actual impact date, impact velocity, and trajectory are known now that DART has launched (see Section 1). However, these are not expected to meaningfully change the outcomes from the shape modeling tests versus the performance we expect from shape modeling in flight.

The simulations for the Bennu cases come in two flavors: “ideal” and “error.” In ideal cases, the spacecraft trajectories of DART and LICIAcube, as well as the Dimorphos ephemeris, match the baseline trajectory and Dimorphos ephemeris described in the previous paragraph. The pointing in the ideal cases ensured that Dimorphos was always in the center of the images, the DART high-gain antenna pointed to Earth, and the solar panels toward the Sun. The error case used a different spacecraft trajectory. The error trajectory deviated from the baseline trajectory by the current best estimate of $1-\beta$ uncertainty in the knowledge of the location of the spacecraft: about 15 m equally to the x -, y -, and

z -coordinates of the spacecraft in the Dimorphos body-fixed frame. For the “error” cases, the pointing changes from image to image to emulate how DART is expected to perform, because the spacecraft does not have reaction wheels and adjusts pointing using thrusters. The error attitude files assume a pointing knowledge of 0.1 mrad $1-\beta$. Because of these differences, the error case and ideal case have different impact locations on the shape model (Figure 6).

Neither case includes errors in the rotational parameters of Dimorphos. The images that will be of a fine-enough scale to use for SPC shape modeling will be taken over a period of <2 minutes, and the rotation of the body during that time is negligible. So, errors in rotational parameters will not meaningfully affect the results of DART shape modeling efforts. Regarding the knowledge accuracy of rotational parameters, the DART team currently assumes that Dimorphos is tidally locked (Rivkin et al. 2021). Consequently, we assume that the spin period of Dimorphos equals its orbital period and that the rotational pole is the same as the orbital pole. The orbital period is $= 11.921624 \pm 0.000018\text{ hr } 3\sigma$ (Scheirich & Pravec 2022). The ecliptic coordinates of the orbital pole in the equinox J2000 are $LP, BP = (320.6 \pm 13.7\ 3\sigma, -78.6 \pm 1.8\ 3\sigma)$ (Scheirich & Pravec 2022). The DART team currently assumes zero libration.

4.3. Ray Tracing

Each simulated image was created by tracing a single ray from the center of each DRACO binned pixel or LEIA unbinned pixel aimed toward Dimorphos. Only a 512×512 pixel window of each DRACO image was used in order to match the dimensions of images that will be streamed to Earth during the Terminal phase. For LEIA, we traced rays from each pixel in the full 2048×2048 pixel image. Our single-ray-tracing method is simple. We assume the camera possesses no distortion and is unaffected by stray light. The simulated images do not contain photon noise, readout noise, or other sources of noise. The performance of both cameras will be thoroughly assessed during flight, and shape modeling efforts will use calibrated images. Ground calibration efforts revealed very low noise and excellent optical quality. We then compute the expected brightness of each pixel at the intersection of the ray with a surface facet using a lunar-Lambertian photometric function (McEwen 1996):

$$I = a_b \left((1 - \varepsilon) \cos i + \varepsilon \frac{\cos i}{\cos i + \cos e} \right), \quad (1)$$

where I is the intensity, i is the incidence angle, and e is the emission angle; a_b is the albedo, and $\varepsilon = e^{-\alpha/\alpha_0}$ is a weighting term between the Lambertian and Lommel–Seeliger reflectance models (where α is the phase angle in degrees and $\alpha_0 = 60^\circ$). The emission angle is computed by taking the dot product of the facet surface normal with the pixel ray, while the incidence angle is determined from the dot product of the Sun vector with the facet surface normal. Other studies (e.g., Barnouin et al. 2020; Weirich et al. 2022) have used more than one ray per pixel, and then convolved the results with a point-spread function for the camera. This more complex and realistic modeling technique produces simulated images with enhanced details that look more like those we expect to obtain in flight. Our simpler approach tends to return blockier and less crisp images but renders images much faster. In simulated images where the pixel scale exceeds the sizes of individual facets in the shape model used to render the images, the resulting blockiness provides an extra level of conservativeness to the resulting DTMs we develop in the tests discussed here. The nature of the simulated pictures prevents extracting subpixel information that would be possible using multiple real images, which are slightly shifted relative to one another, as happens for most images acquired by spacecraft.

The simulated images have an additional limitation: in the highest-resolution simulated images, the pixel scale of the image is smaller than the typical projected size of facets in the truth shape model. Images with a finer pixel scale than a facet give multiple pixels with the same radiance: they essentially have a pixel scale comparable to the average facet size, despite the nominal pixel scale of the image. Using the Itokawa truth model, this occurs for images with a pixel scale finer than 15 cm. For the Benu model, this occurs for images with a pixel scale finer than 28 cm. The finest-scale maplets used in the shape modeling tests have a 10 cm GSD, which is finer than the average facet size for both the Itokawa and Benu truth models. This introduces an additional level of conservatism to the tests. In flight, the highest-resolution image of Dimorphos will truly have a pixel scale of at or better than 10 cm. So, we

should be able to better resolve finer-scale topographic details from flight images than we do in these tests.

5. Results of Shape Modeling Tests

In this section we report comparisons between the reconstructed models and the input images, the internal metrics computed by SPC, and the accuracy of impact site identification, asteroid volume, and impact site tilts for each test.

Figure 7 shows the reconstructed shape models for the Itokawa_DRACO, Itokawa_DRACO+LEIA, Benu_ideal, and Benu_errors tests. The figure shows six views of each model, oriented along the principal X -, Y -, and Z -axes.

5.1. Comparisons to Images

Figures 8 and 9 compare DRACO and LEIA images, respectively, to the starter triaxial ellipsoid and the final shape model. (LEIA images are available for comparison only for the Itokawa_DRACO+LEIA test.) In all cases, the final shape is a much better match to the image than the starter shape. The starter shape was a triaxial ellipsoid with the axial ratios of Dimorphos (ellipsoid), Itokawa (Itokawa_DRACO, Itokawa_DRACO+LEIA), or Benu (Benu_ideal, Benu_errors). The axial ratios of Dimorphos for the ellipsoid test are from the mission DRA for Dimorphos (see Appendix in Rivkin et al. 2021). The axial ratios for the Itokawa tests came from Lowry et al. (2005). The axial ratios for the Benu tests are from Nolan et al. (2013).

We can match the overall scale of the shape model by comparing the extent of the model directly to the image, even in the ellipsoid test. We found that the lack of features in the ellipsoid truth model prevented successfully tiling with maplets. Therefore, the final shape in the ellipsoid case is a triaxial ellipsoid made without using any maplets. In practice, every asteroid seen to date has surface features (Pajola et al. 2022, this focus issue), so the ellipsoid case is not representative of what we expect of images of Dimorphos.

For the Itokawa and Benu tests, we successfully generated topographic features that align with corresponding features in the images for areas where we have images of the lit surface. Unsurprisingly, we have a hard time modeling terrain along the terminator. As maplets approach the terminator, SPC must infer the slopes of unlit areas based on the Sun’s direction and the heights of surrounding lit terrain. Areas that are always in shadow will never be modeled accurately. This is a fundamental limitation of image-based shape modeling from high-speed flybys, and not unique to DART.

In all cases, the final shape models match the limbs seen in the image reasonably well. Smaller details, such as rocks on the limb of Benu, are hard to capture, but large rocks such as the one seen in Figure 8 near twelve o’clock in the Benu cases do manifest themselves in the shape. Keep in mind, however, that the DRACO limb is essentially identical in every image as DART zooms in on Dimorphos. LEIA provides a few unique views of limbs (Figure 9), though in practice ejecta might obscure some or all of them. The ability to match the limited set of limbs visible in the images means that we are matching the bulk shape reasonably well in that particular trace of the shape.

We employed quantitative image-shape-model comparison metrics developed for the OSIRIS-REx mission (Al Asad et al. 2021). These metrics are limb/terminator differences, feature matching, and feature distance. The limb/terminator approach

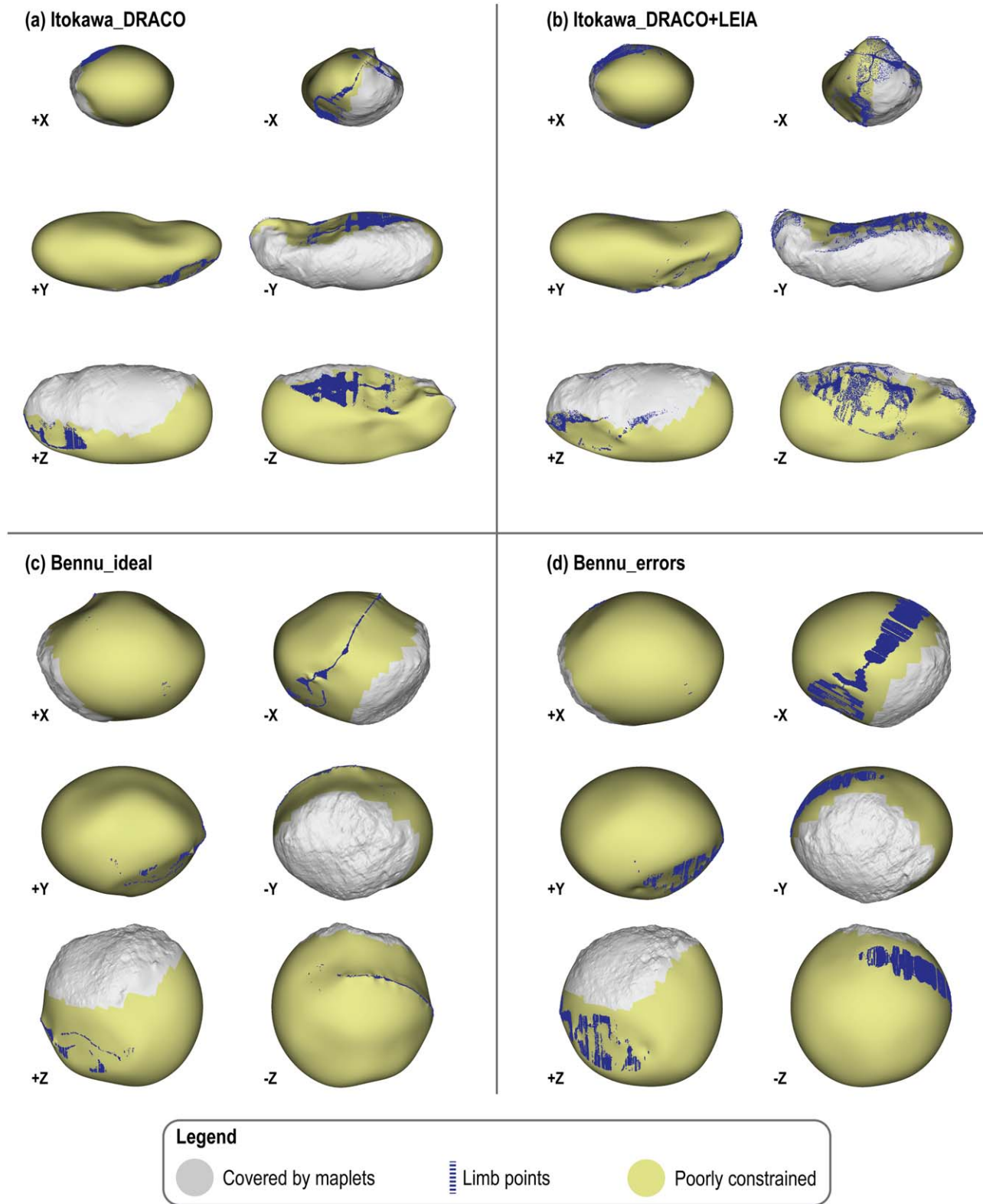


Figure 7. Reconstructed shape models made from simulated images, colored by the type of information used to constrain the shape in a given area. Due to the limited images, only a fraction of the body could be tiled with maplets (gray regions). Limb points (blue) provided additional constraints in a few areas. Scattered points from a single limb (e.g., the Bennu_errors case) indicate errors in the shape model in that location. The bulk of the shape (yellow) was imaged at a high emission angle, was hidden in the dark, or represents unseen portions of the body.

analyzes the positions of the limb and terminator in a rendered image of the shape model versus the real image (i.e., compares the right and left columns of Figure 8). The terminator and limb are identified in the same way for both the reference image and

the reconstructed shape model image by identifying the darkest regions in the image as either space or unilluminated surface. In the case where the shape is perfectly surrounded by limbs, i.e., imaging at low phase, this approach provides a measure of

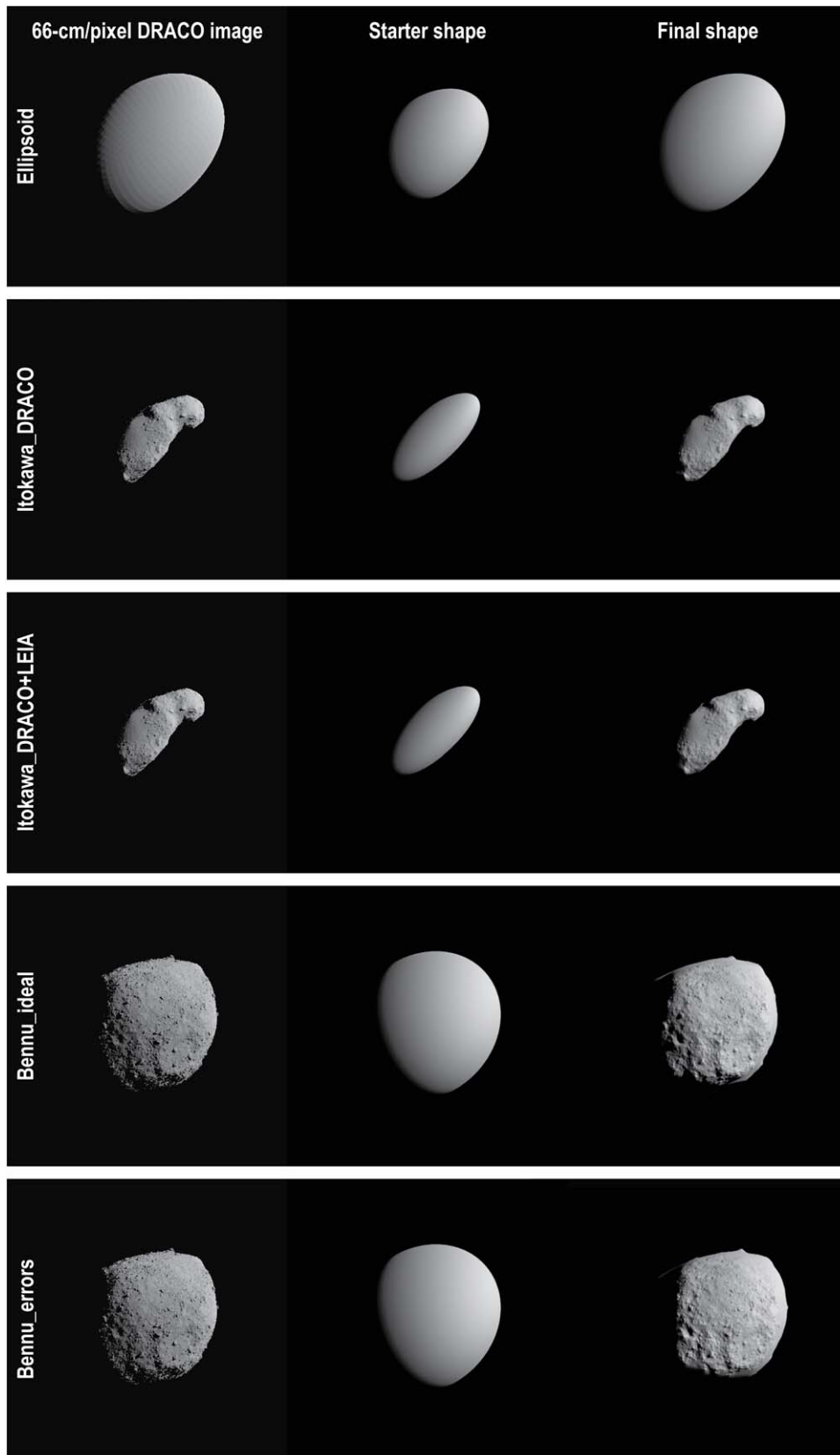


Figure 8. Comparison between the simulated 66 cm-scale DRACO images (left), starter shape model (center), and final shape model (right). The final model matches the image much better than the starter model.

overall shape model accuracy and any potential size bias in the model. If a portion of the surface is a terminator, as is the case with these images, this approach should be an upper bound on

the scale error of the model versus the image. The feature-based methods rely on an automated matching of features, or keypoints, in the images to identify whether the model is too

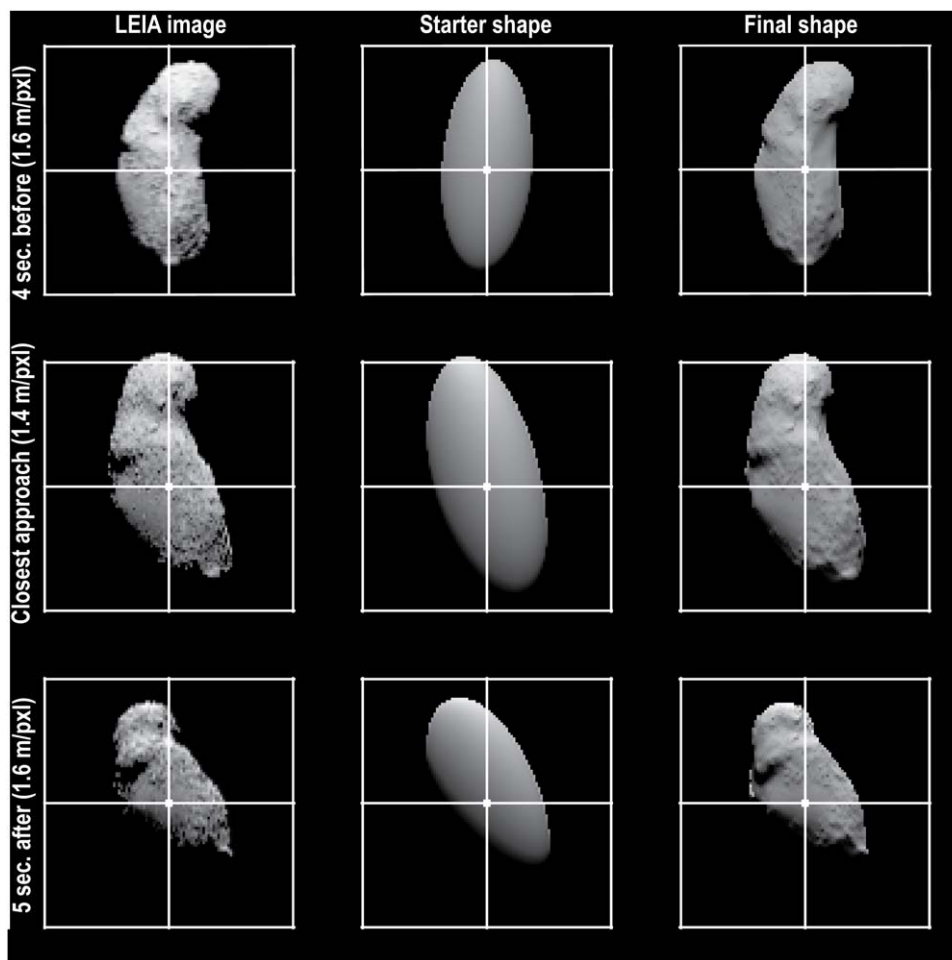


Figure 9. Comparison between three LEIA images around time of closest approach (left), the starter shape (center), and final shape (right) for the Itokawa_DRACO+LEIA test. The image shown here is a 128×128 frame windowed from the 2048×2048 image. In flight, these images could contain ejecta. Grid lines are 50 pixels apart.

big or too small (see Al Asad et al. 2021 for details). The rendered image is rotated, translated, and scaled to minimize the differences of the matched features in the rendered image versus real image. The distances between all features identified in the rendered image are compared against the distance between the corresponding features in the real image. Figures 10 and 11 illustrate the comparisons. Together, these feature-based approaches give measures of model size bias.

Because all DRACO images are effectively the same view, we assessed only the last several images containing the entire body. The LEIA images (used in the Itokawa_DRACO+LEIA test only) also provided a limited (but different from DRACO) range of viewing geometries, and the used images span these geometries. The limb/terminator approach yielded uncertainty for the SPC-derived model sizes ranging from -1.71 ± 0.34 m (1β) to 3.23 ± 0.34 m (1β), depending on the specific test. The maximum size uncertainty amounts to 0.6% of the volume-equivalent diameter of Dimorphos. The reconstructed model is not capturing correctly the long-wavelength tilt of the shape in the terminator region into and out of the image plane, relative to the real model. This error is seen most evidently with the Bennu shapes. In Figure 10, for example, some areas marked as terminators in the Bennu_ideal test are identified as features, not terminators, in the reference image, because the Bennu reconstructed model falls off more quickly. The opposite occurs for the Bennu_errors case: lit terrain in the image is

flagged as being beyond the terminator, but in the shape the terminator is located beyond the terrain. Here, the reconstructed model falls off more quickly than the truth model. These inconsistencies in terminator identification between reference image and shape model are indicators that the Bennu model has the greatest uncertainties in its long-wavelength structure into and out of the image. In the Itokawa and ellipsoid tests, the algorithm does a more consistent job of identifying the same parts of the image as beyond the terminator because the model and reference image match better. The size uncertainties in those tests space a much smaller range of -0.17 ± 0.38 m to 0.72 ± 0.20 m, or no more than 0.4% the volume-equivalent diameter of Dimorphos.

Keep in mind, however, that the uncertainties in shape model scale reported in this paragraph are based on comparisons of the reconstructed model relative to the truth shape *as seen in the image*. The limb/terminator comparison cannot constrain errors in the unseen parts of the shape. See Section 5.3 for further discussion of errors in shape model volume.

The feature-matching and feature-distance methods indicate good agreement in the sizes of the models and reference images, with model-to-image scale factors ranging from 0.998 ± 0.005 to 1.0074 ± 0.002 , depending on the specific test. The median difference between features in the reference image and rendered shape ranges from -0.28 to 0.23 m, which provides another measure for the errors in shape model scale.

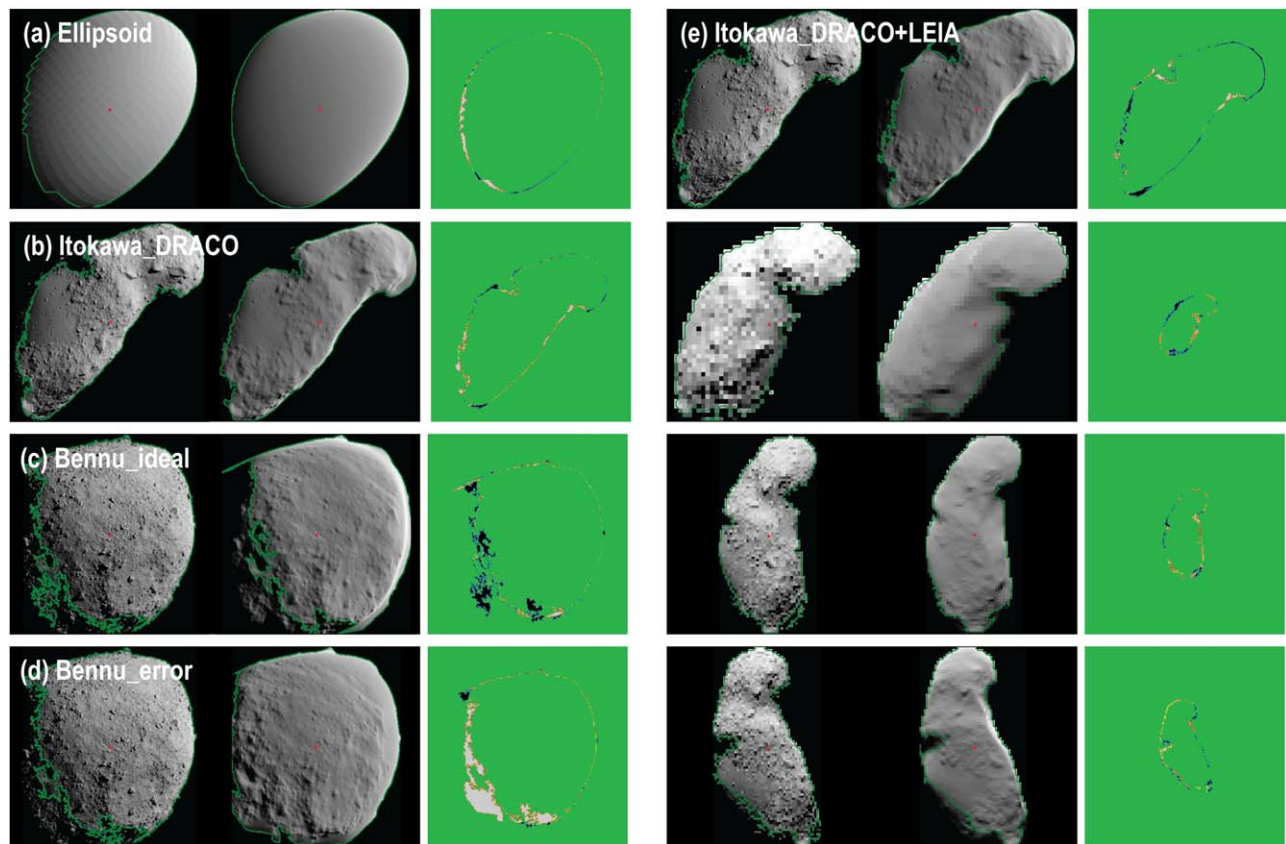


Figure 10. Examples of comparisons between the limbs and terminators of rendered images of the shape model vs. reference images. For each image-model pairing, the left column is the image and the center column is the rendered shape model. Green lines mark the position of the limb and terminator in both. A difference image (right column) emphasizes mismatches between the models and images. Green areas are where the model and image agree; other colors indicate areas of mismatch. All four images in the right panel are from the Itokawa_DRACO+LEIA test. The top image is from DRACO; the following three are from LEIA.

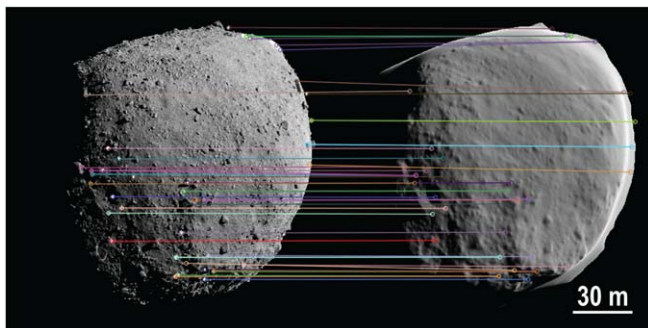


Figure 11. Example of keypoint identification. The algorithm identifies features (keypoints) in the reference image and rendered shape model, which here are shown as dots connected by colored lines. The algorithm then compares the distances between all the keypoints in the reference image and rendered image to assess the shape model.

Table 3 summarizes the results of the image/model comparisons for each test. In all cases, much of the difference occurs at the terminator rather than the limb. This concentration of errors near the terminator indicates errors in the overall curvature of the model, which is to be expected given the minimal stereo available.

In summary, the reconstructed models match the features and limbs in the images quite well, especially considering that we are effectively modeling the shape from a single image (or redundant set of images) for DRACO and a handful of images from LEIA, when available. The terminator is consistently difficult to match, in large part because we have no data in the

shadows. The reconstructed shape matches the size of the body in the image better than or equal to 0.7% the volume-equivalent diameter of Dimorphos on the basis of limb/terminator, feature-matching, and feature-distance assessments. Mismatches are largely due to long-wavelength tilts not being captured well into and out of the image, especially near the terminator.

5.2. Internal SPC Metrics

SPC contains various internal metrics that can be used to get a sense for shape model quality (Al Asad et al. 2021; Palmer et al. 2022). However, due to the nature of the DRACO data set some of these metrics are not as useful as they would be with a broader set of images. In particular, the formal uncertainty metric is a good measure of model quality with ideal imaging conditions (Weirich et al. 2022), but that metric breaks down in the absence of meaningful stereo and provides useful information only when LEIA images are included. Two other metrics, the rms residual per maplet and sigma, are measures of internal consistency. The rms residual per maplet provides a measure of the goodness of fit for each maplet based on each image in the maplet. Sigma is the standard deviation of the heights in overlapping maplets. Neither rms residual per maplet nor sigma is well suited for identifying systematic offsets in the model versus truth (e.g., an error in the overall position of the model).

Table 4 lists the values of these metrics for each test that involved maplets. Figure 12 shows the distributions of these

Table 3
Quantitative Comparisons between Images and Reconstructed Models

Test	Limb/Terminator Size Uncertainty (m)	Scale Factor (Model to Image)	Median Difference between Features (m)
Ellipsoid	0.72 ± 0.20 rms = 0.74	N/A	N/A
Itokawa_DRACO	0.45 ± 0.25 m rms = 0.51 m	1.001 ± 0.002	-0.05
Itokawa_DRACO+LEIA	-0.17 ± 0.38 rms = 0.41	1.007 ± 0.005	-0.28
Bennu_ideal	-1.71 ± 0.34 rms = 1.74	1.002 ± 0.006	-0.01
Bennu_errors	3.23 ± 0.34 rms = 3.17	0.998 ± 0.005	0.23

Table 4
Internal SPC Metrics^a

Test	rms Position Uncertainty (m)	rms Residual (m)	Mean Sigma (m)
Itokawa_DRACO	Not meaningful	0.06	0.02
Itokawa_DRACO +LEIA	8.52 ^b	0.19	0.02
Bennu_ideal	Not meaningful	0.08	0.02
Bennu_errors	Not meaningful	0.06	0.03

Notes.

^a ideal1_draco is not shown because no maplets were generated in that test.

^b Based only on the landmarks that included LEIA images.

metrics across the final shape models. The rms position uncertainty is only meaningful for the test that included LEIA images and for maplets that contain both DRACO and LEIA images. The landmarks that contain both DRACO and LEIA images in Itokawa_DRACO+LEIA have a mean rms position uncertainty of 8.5 m. The rms residual ranges from 6 to 11 cm, depending on the test. This length scale is similar to the pixel scale of the finest-scale images in the model. The mean sigma is between 2 and 4 cm, depending on the model. Larger values tend to occur near the edge of maplet coverage. The small values for these latter two metrics indicate that the images and maplets are all in good agreement with one another. However, given the quality of images for DART versus ideal SPC imaging conditions, that high level of self-consistency is not necessarily an indication that the model has decimeter- or centimeter-scale accuracy. The precision in terms of matching imagery, however, is good.

5.3. Comparisons to Truth Models

While comparing the truth and reconstructed models, keep in mind that the majority of the truth shape is never seen in either DRACO or LEIA images. Only about half the body is lit at the time of the DART impact, and neither camera sees the entire lit surface. In flight, the images themselves are the sole source of truth. For the purposes of the shape modeling tests, however, we can compare the reconstructed shape models to the truth models used to simulate the images and assess how well we can reconstruct the bulk shape, given the limited imaging afforded by DART.

Figures 13–15 compare the truth and reconstructed models for the ellipsoid, Itokawa_DRACO, and Bennu_ideal tests. Figure 16 compares the Itokawa_DRACO+LEIA reconstructed shape to the DRACO-only Itokawa_DRACO shape and truth shape. Figure 17 compares the Bennu_ideal and Bennu_errors reconstructed shapes against each other and against the truth shape. The smooth areas of the reconstructed shape models (especially visible in the +Z, -X, +Y, +Z, and -Z views) are areas that were never seen in images. No

features are seen in these areas because the shape-reflection process and subsequent steps involve coarse shapes.

In the ellipsoid test, the reconstructed shape is uniformly slightly smaller than the truth shape in all views (Figure 13). The aspect ratios of the truth and reconstructed shapes are identical, so the offset between the two shapes is constant everywhere.

In Itokawa_DRACO, the reconstructed shape protrudes beyond the truth shape in some areas, but it is too small in others. With the exception of the one limb seen by DRACO (which creates the ridge in the +x view in Figure 14(b)), the “head” is too small. The “belly” does not curve in adequately, as manifested by the excess blue material visible along the belly in the +Y and -Y views of Figure 14(b). (Annotations on Figure 14(b) indicate the location of the neck, belly, etc.) Neither does the “neck” of Itokawa, as can be seen in the +Z and -Z views of Figure 14(b). The “shoulder” visible near seven o’clock in the -Y view in Figure 14(b) does not stand tall enough in the reconstructed shape. Most of the belly is never seen, which explains the excess material in the +Y and -Y views. The neck and shoulder are more interesting: parts of these are visible in the DRACO images, and in the images these features align nicely with corresponding features in the shape model, much as the ridge on the head in the -X view matches the DRACO limb. However, the lack of stereo and limited viewing conditions leads to errors in the long-wavelength topography of these features into and out of the image plane (as seen with the above terminator discussion). Instead, the fine-scale topography remains largely latched to the surface of the starter shape. In the absence of a truth shape model and with the single view from DRACO, we can only suspect that these areas stuck out too far (like the neck) or not far enough (like the shoulder and head) from the threshold/terminator assessments. Overall, for this test case, the areas where the reconstructed shape is too large approximately balances out where it is too small. In Bennu_ideal, the reconstructed shape model extends beyond the truth model in most areas. The fine-scale features are offset from where they should be on the truth model, despite the excellent match between the reconstructed model and the image in many areas (Section 5.1). The -Z view in Figure 15(c) is a good example of this offset. The reconstructed shape (blue) is located above the truth shape, but it shows similar features in offset locations. As with the Itokawa case, the finer-scale topography latched on to the starter shape and, in the absence of stereo, does not know it needs to move. The starter shape was almost uniformly too large everywhere, despite having axial ratios based on radar data. This occurred because the shape of Bennu is faceted and diamond-shaped, whereas the triaxial ellipsoid is convex everywhere. The topography ends up being built as deviations with respect to the convex ellipsoid surface, rather than on subplanar surfaces.

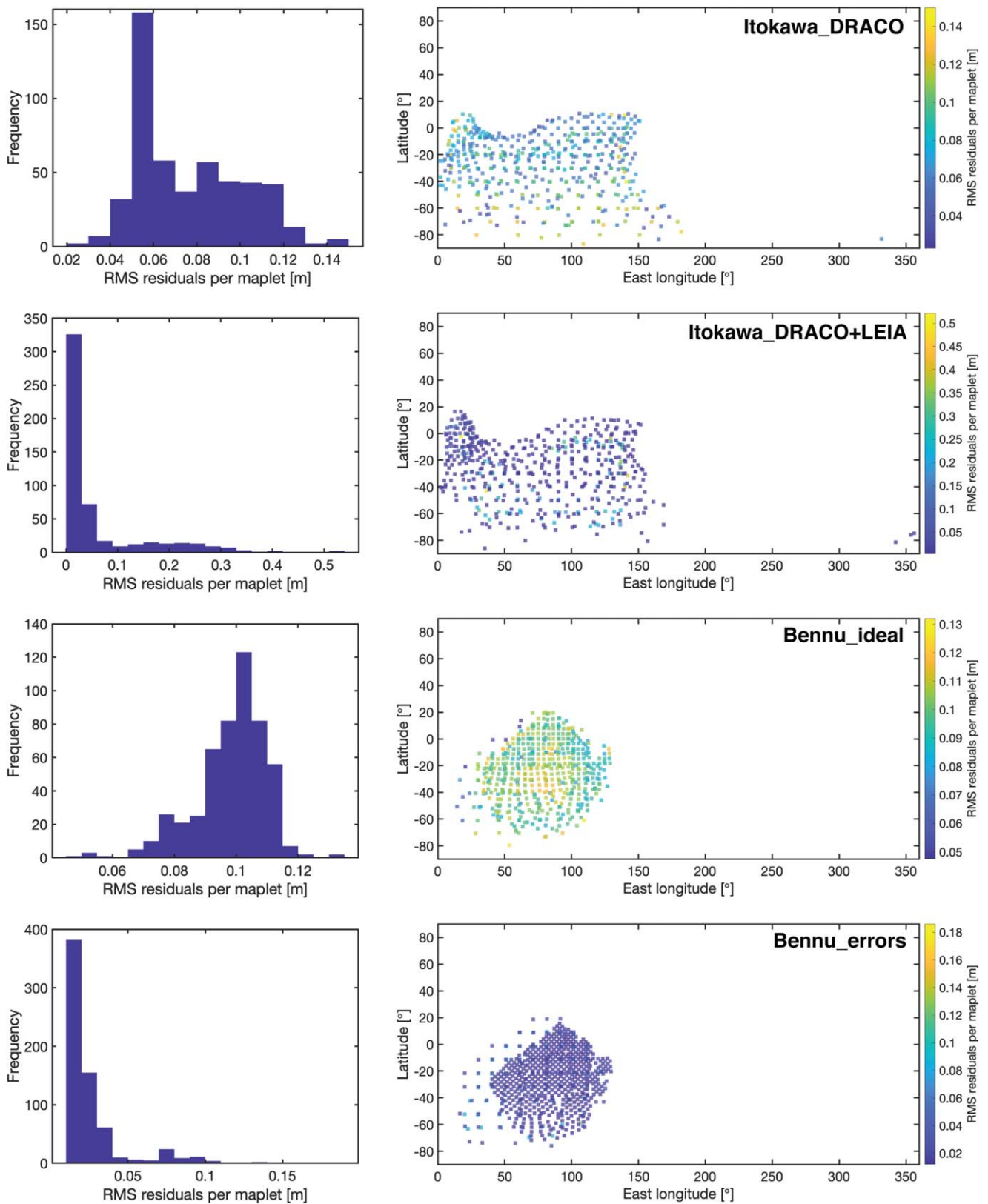


Figure 12. Comparisons between the rms residual per maplet for the four test tests with maplets. For the Itokawa DRACO+LEIA case, the maplets with the higher rms residuals are the maplets that contain both LEIA and DRACO images, in part because of the coarser pixel scale of the LEIA images, because LEIA images are only in the coarsest maplets, and because DRACO images are redundant views at progressively higher resolution, which all agree with each other very well. In both Itokawa tests, higher residuals in DRACO-only maplets tend to occur at the edges of maplet coverage where the image fades off into terminator or is high emission near a limb.

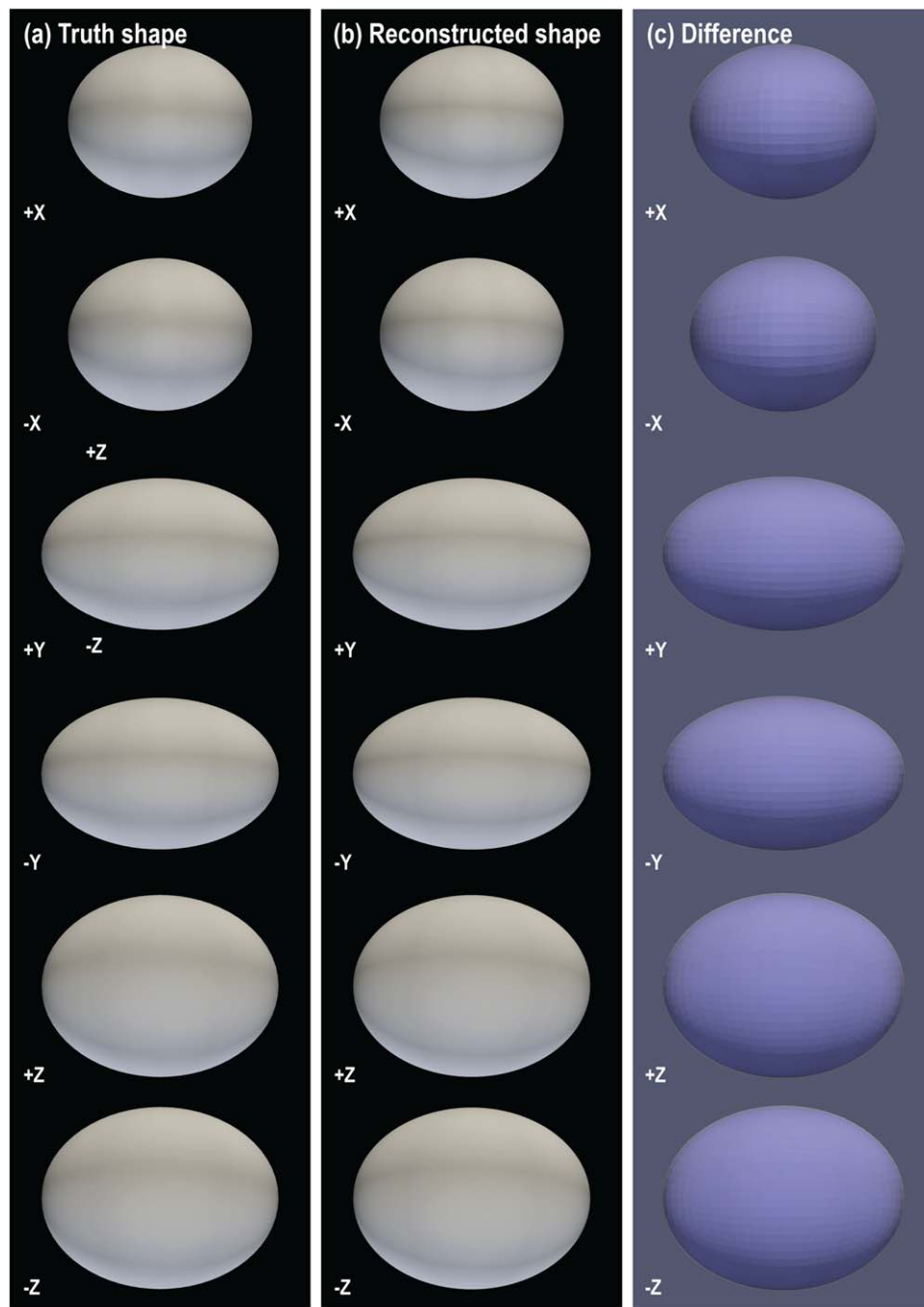


Figure 13. Comparison between the truth and reconstructed shape models for the ellipsoid test. In the rightmost panel, the truth shape is colored ivory and the reconstructed shape is blue. The shapes in that panel all appear a light blue color because the reconstructed shape model is always slightly inside (i.e., slightly smaller than) the truth shape.

Figure 16 shows the added shape information contributed by LEIA images. The majority of the body remains neither visible nor illuminated even with the inclusion of LEIA images. Nevertheless, the limbs from the images are powerful. Compare, for example, the $-X$ views in Figures 16(a) and (b). That view in Figure 16(b) is much more rounded and head-like, whereas the view in Figure 16(a) has a ridge that comes from the sole DRACO limb of the head. The improved curvature of the head in the $-X$ view comes not from standard maplets, but rather from limb-only maplets. The LEIA limbs also help to sculpt the belly inward from the Itokawa_DRACO test. This improvement is clear in the $+Y$ and $-Y$ views of

Figure 16(c), where the yellow shape from the test with LEIA images is a much better match to the ivory truth model than the red DRACO-only model. Once again, this improvement stems not from standard maplets, but rather from improved trimming because we have additional constraints on what is *not* seen. The stereo provided by LEIA is not adequate to snap the yellow topography to the truth shape in areas such as the neck and shoulder of Itokawa, in large part because LEIA images cannot go in the majority of landmarks, but it does help a little bit. The fine-scale topography is also relatively unchanged compared to the DRACO-only case due to the low resolution of the LEIA images. But, the limbs from LEIA provide helpful constraints

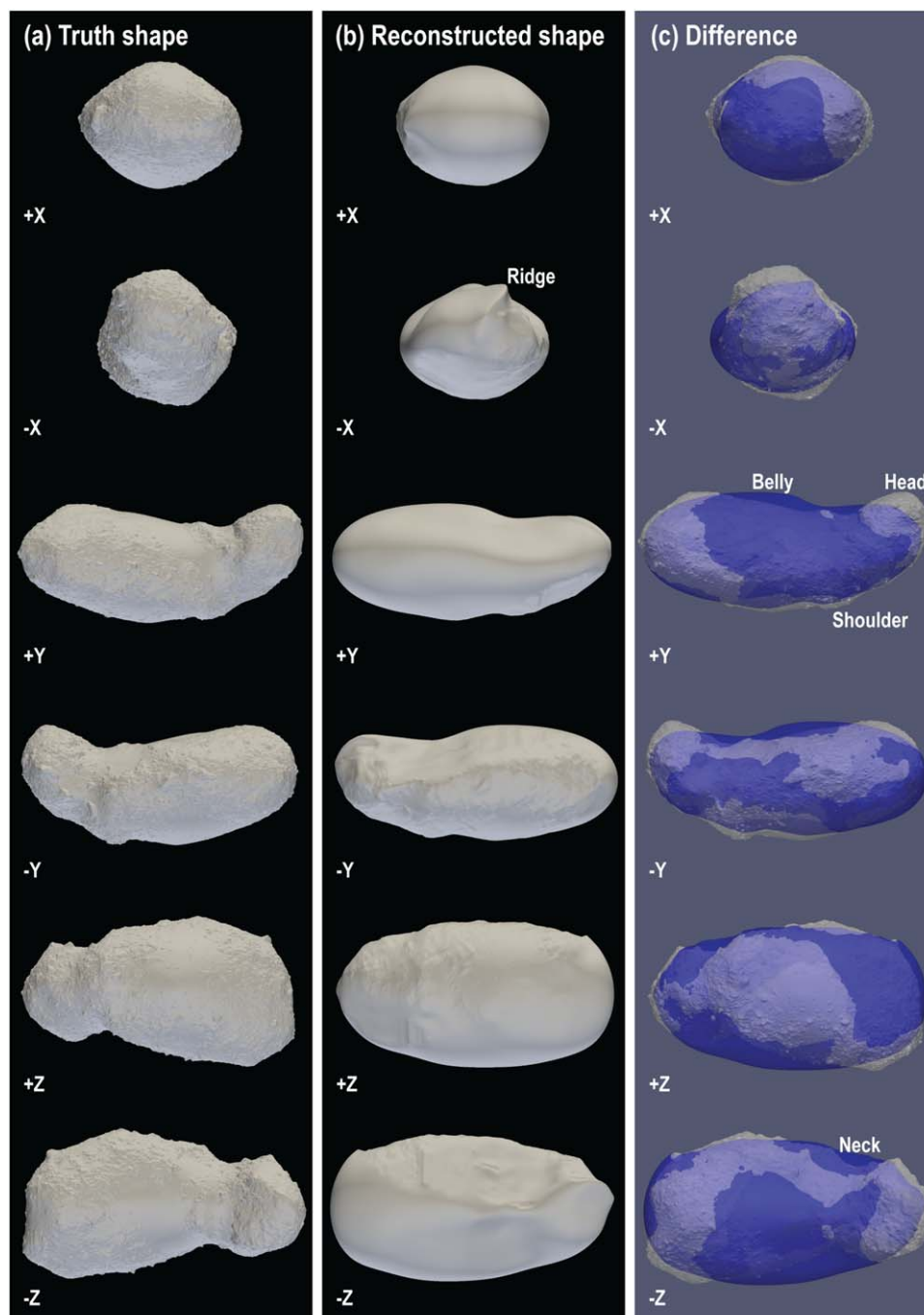


Figure 14. Comparison between the truth and reconstructed shape models for the Itokawa_DRACO test. The figure shows six views along the principal X -, Y -, and Z -axes of the shape models. The $-Y$ view is the side that is best seen by DRACO. In the rightmost panel, the truth shape is colored ivory, the reconstructed shape is blue. In some places the blue shape extends beyond the truth shape (e.g., the underside of the “belly” of Itokawa in the $+Y$ and $-Y$ panels). In other places, the reconstructed shape is too small (e.g., the “head” of Itokawa in the $-X$, $+Y$, and $-Y$ panels). In terms of overall volume error, the places where the reconstructed shape extends too far compensate for the places where the reconstructed shape does not extend far enough. This offset helps make the overall volume error low, despite the mismatch in bulk shape in unseen areas. Figure 7 shows which areas are constrained by maplets or limb points.

on the bulk shape through both limb-only maplets and trimming information.

Figure 17 compares the reconstructed shape models for the Benu_ideal and Benu_errors cases. Keep in mind that the trajectories differ between the two cases, with the error trajectory biasing the highest-resolution images toward the terminator. We know that the shape model performs more poorly near the terminator than in well-lit areas. Differences in the bulk shape for the ideal and error cases are apparent,

particularly when viewing the shapes in the $+X$ and $-X$ directions. This particular difference stems not from the errors in spacecraft position and camera pointing, but rather to a large trim being done to the ideal case but not to the error case. This was a judgment call made by the modeler—and the fact is that, in the absence of images of these areas, shape modeling is partly a judgment call. Hence, the differences in the locations of fine-scale topographic features in the reconstructed shapes is likely due not to the errors in spacecraft position and camera

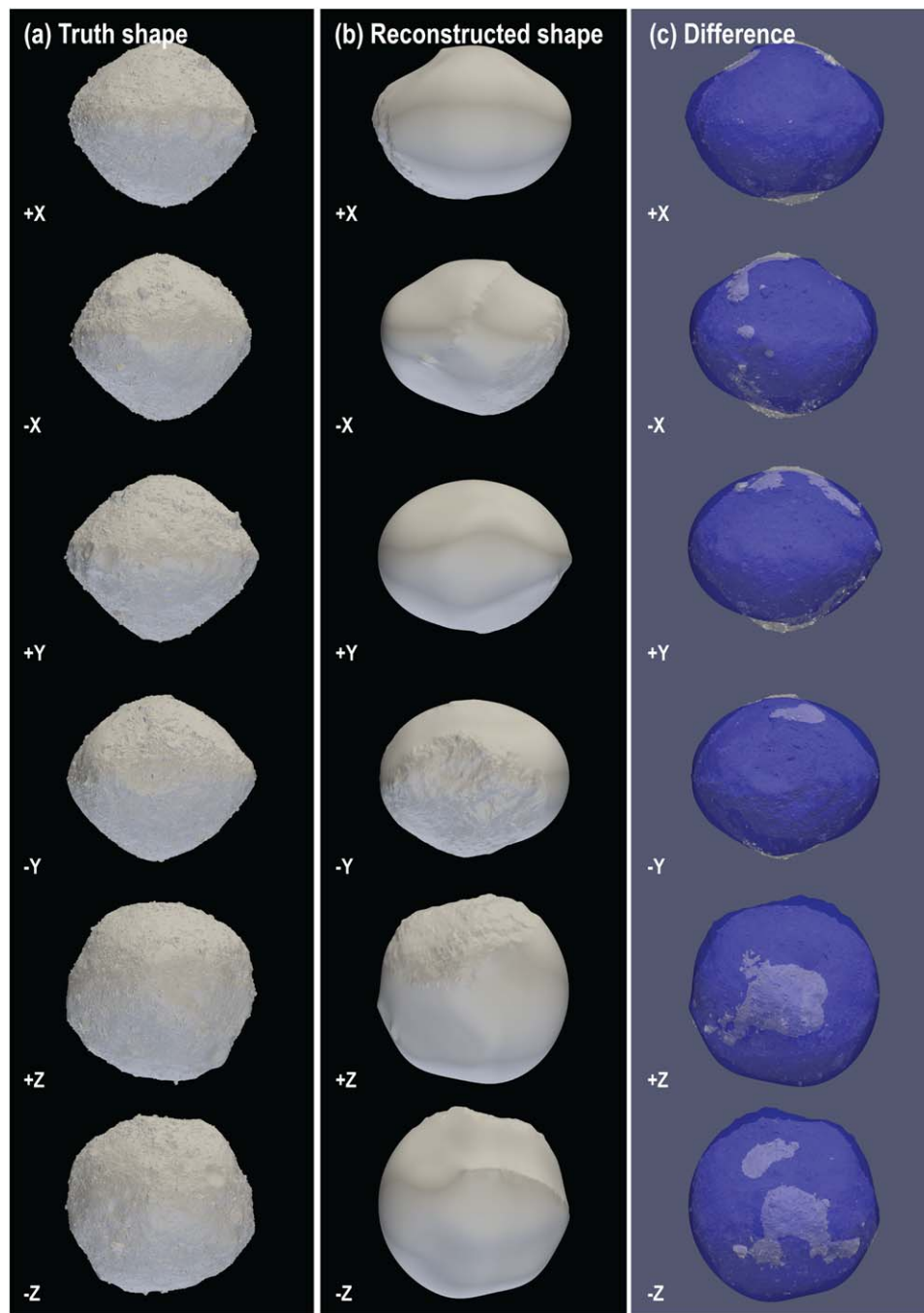


Figure 15. Comparison between the truth and reconstructed shape models for the Bennu_ideal test. The figure shows six views along the principal X -, Y -, and Z -axes of the shape models. The $-Y$ view is the side that is best seen by DRACO. In the rightmost panel, the truth shape is colored ivory, and the reconstructed shape is blue. In contrast to the Itokawa case, in the Bennu case the reconstructed shape model is almost uniformly too large (i.e., the blue protrudes beyond the ivory in the vast majority of places). Figure 7 shows which areas are constrained by maplets or limb points.

pointing, which SPC can readily correct, but rather by the limitations inherent in the single view afforded by DRACO images. The differences in the reconstructed shapes between Bennu_errors and Bennu_ideal provide a sense of the challenges of building shape models from the DART data set, as well as the influence of the starter shape in the absence of meaningful stereo.

Figure 18 emphasizes the extent to which topography latches to the starter shape. Figure 18 shows the $-Z$ views of the Itokawa_DRACO and Bennu_ideal shape models, but focuses on an area of the shape that was imaged by DRACO. DRACO

would be viewing the shape from the direction of the top of the figure. The long-wavelength topography in the reconstructed shape follows the starter ellipsoid, which is why the neck of Itokawa does not dig in deeply enough and the bump near twelve o'clock on Bennu sticks out too far. Without robust stereo to fix the position of features in 3D space into and out of the image plane, the reconstructed topography hews closely to the starter shape. DRACO images allow us to build topography that reasonably models the locations of features in 2D images. But, information on the 3D dimension (i.e., into and out of the page) is missing, and this leads to errors in the location of the

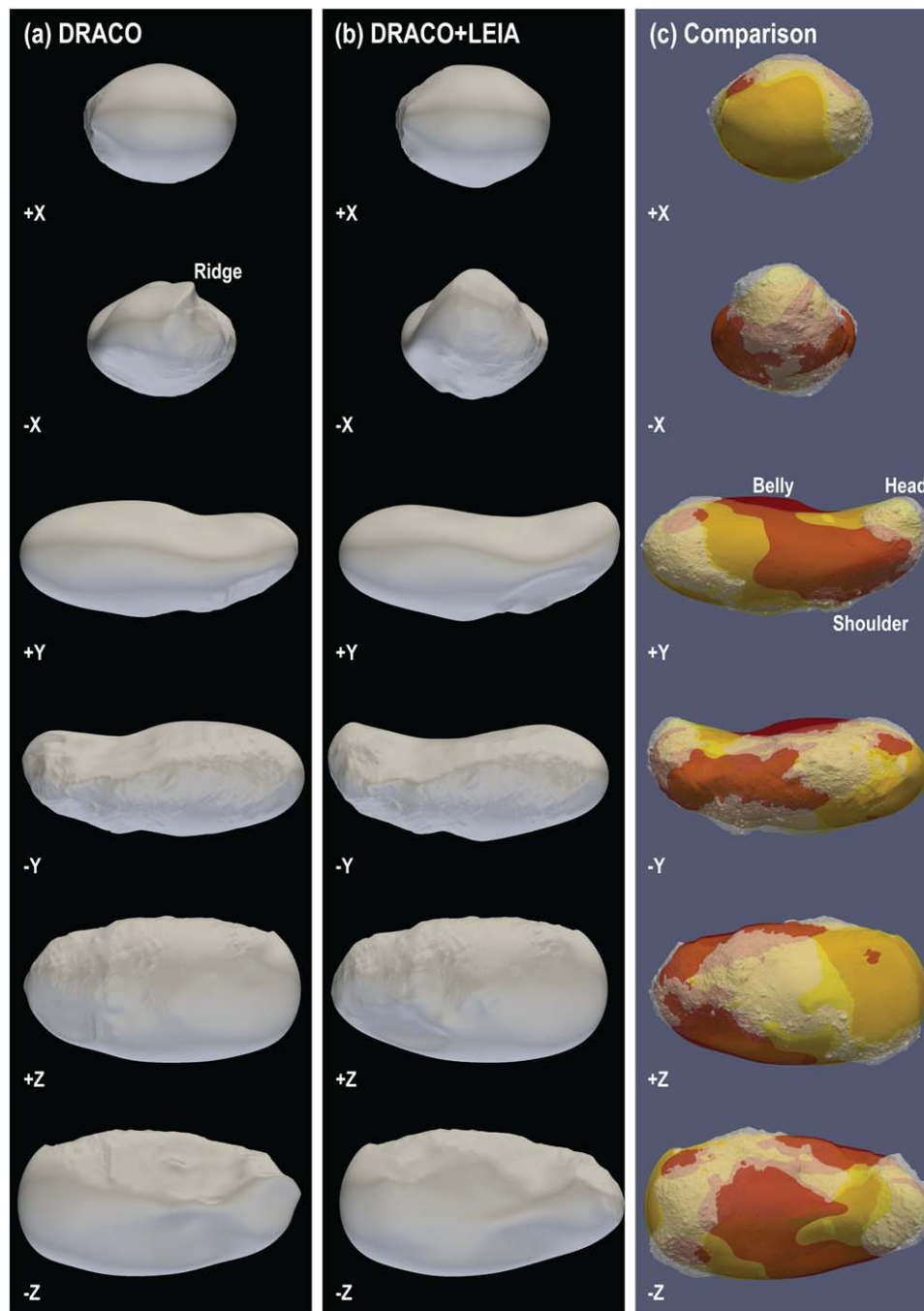


Figure 16. Comparison between the DRACO-only and DRACO+LEIA reconstructed shape models for Itokawa. The figure shows six views along the principal X -, Y -, and Z -axes of the shape model. The $-Y$ view is the side that is best seen by DRACO. In the rightmost panel, the truth shape is colored ivory, the DRACO-only shape is red, and the DRACO+LEIA shape is yellow. The DRACO+LEIA shape is a much better match to the head and belly of Itokawa than the DRACO-only shape. This improvement occurs largely because of the additional limbs provided by LEIA images, which help to bump out the head and carve in the belly. Figure 7 shows which areas are constrained by maplets or limb points.

surface of the shape model in that direction. The limb/terminator assessment will be our primary way of constraining this error in flight.

In summary, comparisons between the truth and reconstructed shape models show that the topography, which aligns nicely with features seen in images, is not placed correctly in 3D space. Instead, the finer-scale topography is latched to the starter shape. LEIA images can help improve the match to the truth shape at long wavelengths, and the differences between

models built from images with and without errors in spacecraft position and camera pointing stem more from the inherent limitations of DRACO images than from the errors themselves. Despite the added information from LEIA images, the comparisons with these truth models suggests that in flight we will need to be wary about long-wavelength topography into and out of the plane of the DRACO images, despite good agreement between rendering of the shape model and the actual images.

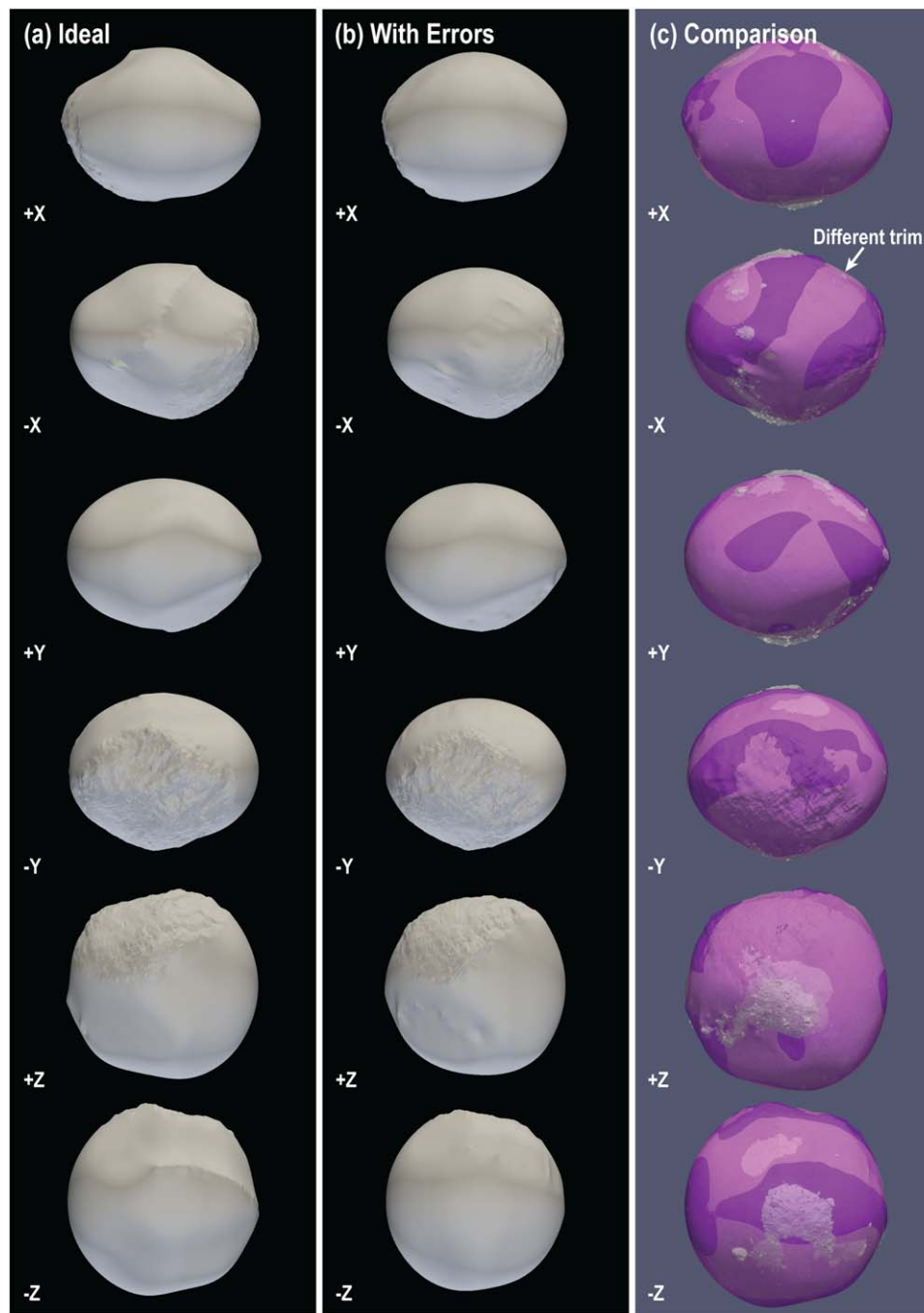


Figure 17. Comparison between final shape models built using (a) images of shrunken Benu with perfect knowledge of spacecraft position and camera pointing, (b) images with expected errors in spacecraft position and camera pointing, and (c) a comparison of both shapes vs. the truth model. In (c), the Benu_ideal model is dark purple, the Benu_errors model is lilac, and the truth model is white. The long-wavelength differences between the shapes are more likely due to differences in trimming (visible in the $-X$ view), rather than errors in camera knowledge. The $-Y$ view is the side that is best seen by DRACO. Figure 7 shows which areas are constrained by maplets or limb points.

5.4. Identification of the DART Impact Site

Figure 19 shows the locations of the impact sites in the five tests and compares the locations of the truth impact site (yellow) and the reconstructed impact site (cyan) in the final image. The Itokawa_DRACO and Itokawa_DRACO+LEIA cases share the same impact site, which corresponds to the wall of an impact crater. The two Benu cases impact different locations on the surface because the images were simulated from different trajectories. The Benu_ideal case impacts among a cluster of boulders, whereas the Benu_errors case

impacts next to a small impact crater. The Benu_errors case impacts ~ 13 m closer to the terminator than the Benu_ideal case.

Comparisons between the truth and reconstructed impact sites show that we will be able to identify the impact site to within < 2 pixels in the final image downlinked by DART (Table 5). This is likely an upper limit on the expected error because the simulated images did not truly achieve the resolution due to the shape model facets being coarser than the pixel scale of the highest-resolution images used to build

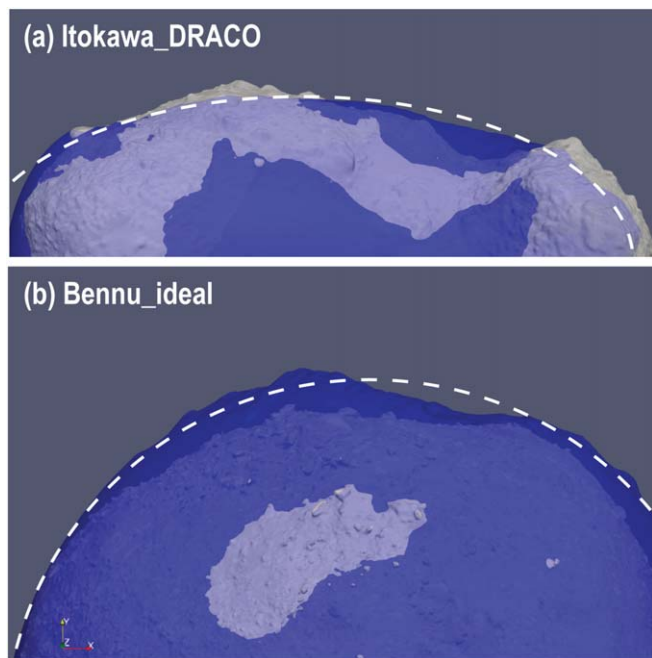


Figure 18. Comparison between the truth (ivory), reconstructed (blue), and starter ellipsoids (dashed white line) as viewed in the $-Z$ direction for a portion of the shape imaged by DRACO. The reconstructed shape hews closely to the starter shape.

the model. Real images will better resolve features (i.e., they will continue to get sharper), and subpixel information will enable more precise image registration. The final simulated images have pixel scales of ~ 10 cm (but see caveat about truth shape model facet size versus image pixel scale in Section 4). So, a < 2 pixel offset corresponds to an error of < 20 cm. This distance amounts to 8% of the size of the DART spacecraft’s core’s maximum envelope (2.5 m). We will know with confidence where DART hit in the final DRACO image, which means we will know definitively whether DART hit a boulder, a smooth region, or some other geologic feature.

In addition to knowing what DART hits in the final image, it is useful to understand the accuracy of the impact site location in 3D space. That assessment provides a sense for the sort of errors we might expect in impact site location relative to the center of the body, which could potentially affect the deflection caused by DART. The offset in 3D space between the truth impact site on the truth shape model and the reconstructed impact site on the reconstructed shape model ranges from 0.7 to 13.7 m (Table 6), depending on the test. Figure 20 illustrates the offset. As discussed in Section 5.3, differences exist in the locations of the surfaces of the truth and reconstructed shapes, and these differences explain the offset of the impact sites in 3D space.

The offset between the truth and reconstructed impact sites is larger in 3D space than in pixel coordinates. This is because in 3D space errors in the overall shape model contribute to the offset. These errors can be larger than the ~ 2.5 m maximum envelope of the DART spacecraft core, and in the largest case amount to being off by about five spacecraft cores. The offset is driven by errors primarily perpendicular to the DRACO image plane in the position and curvature of the reconstructed shape. For DART, the position perpendicular to the DRACO image plane is heavily influenced by the location and curvature of the starting shape model due to the lack of stereo in DRACO

images. However, numerical impact models show that an offset of this scale is unlikely to meaningfully affect the β determination (Stickle et al. 2022, this focus issue; Stickle et al. 2015). The offset in 3D space in these tests is, at most, only about 8% of the volume-equivalent diameter of Dimorphos, and will not be an issue unless DART slams into Dimorphos very near the limb, which is unlikely based on Monte Carlo simulations of the autonomous onboard navigation system on DART. The distance from the limb depends on the shape of Dimorphos, but, for a sphere, the impact would have to be more than 60 m from the center of figure, a distance that is $4.2\times$ larger than the offset in 3D space in the worst-performing Bennu_errors test.

In summary, what matters most is that we will know with excellent accuracy what feature(s) in the DRACO images DART collided with. We will know within < 20 cm where the DART spacecraft hit in the final DRACO images, which means we will be able to use the geologic features in that region to confidently assess the nature of the impact site. Larger errors are expected in 3D space, up to ~ 13 m; but these errors are not large enough to meaningfully affect the interpretation of the DART experiment and stem from the far-from-optimal imaging conditions.

5.5. Estimated Volume of Dimorphos

Table 6 shows the volume errors of our models as compared to the truth models (Figure 21). These results allow us to get a sense of the range of volume errors to expect in flight. Our volume uncertainties range from -2% to $+23\%$. These results indicate that the uncertainty in the density of Dimorphos, which the DART project assumes is 25%, is comparable to or will dominate the uncertainty in β .

In all cases, the shape modeling process improved the volume estimate from the starter models. This indicates that the shape modeling process improves the volume estimate over a simple triaxial ellipsoid based on light curves, even if we see only a portion of the lit body and even though the imaging conditions are far from optimal for SPC. The final shape represents a 20%–95% reduction in the volume error, compared to the starting shape.

In general, the closer the starter shape is to the true volume, the closer the final shape is to the true volume. (The ellipsoid case is an exception: the truth model was an ellipsoid and in matching the illuminated and visible part of the model, we also matched unseen or unlit areas). In the Itokawa cases, the volume errors are so small in part by happenstance. The reconstructed shape models poke out too far in some places but do not stick out far enough in others (Figures 14, 16, and 18). For the Bennu models, in contrast, the starter triaxial ellipsoid was almost uniformly too large (Figures 15, 17, and 18). This offset led to a larger error in the volume of the starter shape for the Bennu cases, which trickled down into a larger error in the volume of the final model.

5.6. Tilts at the Impact Site

The DART spacecraft consists of a “core” with a maximum envelope of 2.5 m, flanked on either side by two long, rectangular solar arrays that measure 8.6×2.3 m. Because of this spacecraft geometry, we consider tilts at two different length scales. The first length scale is 1.8 m, which corresponds to the length across the “box” of the core, whereas the 2.5 m

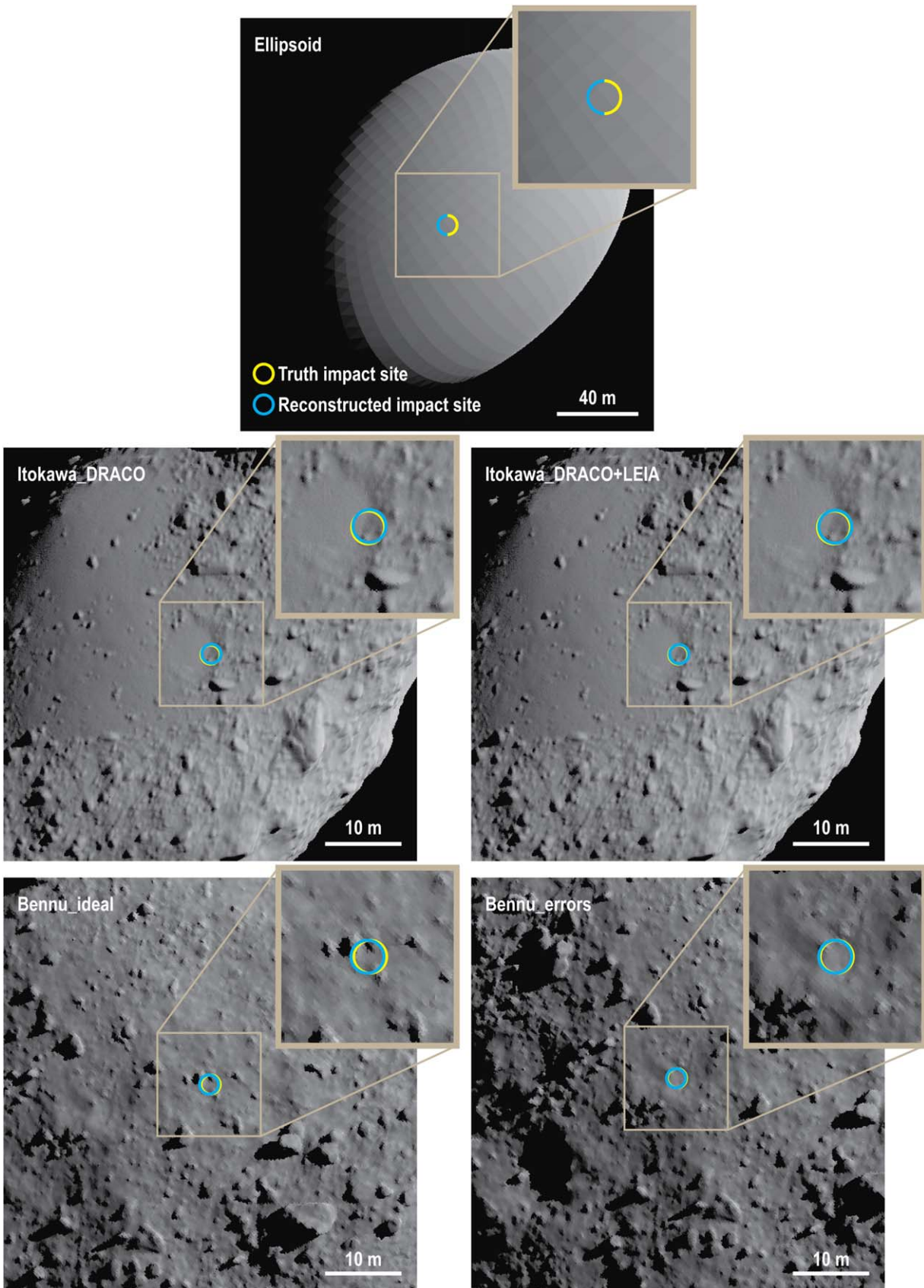


Figure 19. Locations of the truth and reconstructed impact sites in the final simulated DRACO image for each test. Yellow (truth) and cyan (reconstructed) circles are 2.5 m in diameter, which is the maximum envelope of the DART spacecraft core. In all cases, the circles almost entirely overlap, which demonstrates that we will be able to both precisely and accurately identify the impact site, regardless of asteroid shape, whether LEIA images are available, and errors in spacecraft position and camera pointing. The insets are a zoom-in view of the impact site; the geologic context is clear. Although the insets do not have separate scale bars (for clarity of the image), the 2.5 m diameters of the circles provide a sense for scale.

Table 5
Accuracy of Impact-site Location in Final DRACO Image

Test	Truth		Reconstructed		Error		
	Pixel	Line	Pixel	Line	Pixel	Line	Pixel Distance
Ellipsoid	257.2	256.8	257.2	256.8	0.0 ^a	0.0 ^a	0.0 ^a
Itokawa_DRACO	257.1	256.9	258.4	256.5	-1.4	0.4	1.4
Itokawa_DRACO+LEIA	257.1	256.9	258.2	256.3	-1.1	0.6	1.3
Bennu_ideal	257.2	256.7	255.5	256.9	1.8	-0.2	1.8
Bennu_errors	255.1	248.6	253.6	248.5	1.5	0.01	1.5

Note.

^a The pixel, line, and pixel distance errors are zero in this test because no adjustments were made to the image position by building landmarks.

Table 6
Accuracy of Impact Site Location in 3D Space

Test	Truth Impact Site			Reconstructed Impact Site			Offset (m)
	X (m)	Y (m)	Z (m)	X (m)	Y (m)	Z (m)	
Ellipsoid	-0.01	66.4	-37.0	-0.01 ± 0.00	65.80 ± 0.00	-36.65 ± 0.1	0.66 ± 0.00
Itokawa_DRACO	0.00	29.0	-16.2	-2.16 ± 0.1	28.61 ± 0.04	-16.98 ± 0.02	2.34 ± 0.1
Itokawa_DRACO+LEIA	0.00	29.0	-16.2	-2.24 ± 0.1	28.72 ± 0.02	-16.53 ± 0.01	2.29 ± 0.1
Bennu_ideal	-0.01	68.7	38.3	2.96 ± 0.1	77.43 ± 0.01	-39.98 ± 0.1	9.39 ± 0.02
Bennu_errors	-13.3	62.4	-43.1	-10.99 ± 0.1	75.01 ± 0.01	-48.01 ± 0.1	13.66 ± 0.02 ^a

Note.

^a Offset most likely reflects differences in bulk shape related to the proximity of the Bennu_errors impact site to the terminator, rather than the errors in spacecraft position and camera pointing in the images.

maximum envelope includes things such as the antennas that attach to that box. The second length scale is 18 m, which corresponds to the span of the solar arrays. These length scales were chosen based on results from the DART impact modeling working group about the length scales relevant to affecting the outcome of the DART impact (Stickle et al. 2022, this focus issue). Tilts and their calculations are described in detail by Barnouin et al. (2020). Here, tilts of the facets in a shape model are relative to the spacecraft impact velocity vector. Those tilts are then averaged over a region with a radius of 0.9 m and 9 m, respectively, to produce two quantities: mean tilt (which is simply the average tilt of all facets in the region, weighted by the area of each facet) and mean tilt direction (which is the average direction of the tilts, again weighted by the area of each facet). See Barnouin et al. (2020) for the mathematical formulation of these quantities.

Figure 22 shows the distribution of mean tilt across the truth and reconstructed impact models for the Itokawa_DRACO, Itokawa_DRACO+LEIA, Bennu_ideal, and Bennu_errors tests. The mean tilt map for the ellipsoid case is not shown because that test did not generate topography through SPC. The tilt radius of 0.9 m resolves tilt variations that are not apparent in the 9 m radius tilt maps. This difference in detail results from the fact that the 9 m radius tilt map has a ten-times longer baseline. The 0.9 m tilts are sensitive to smaller-scale features on the surface, such as boulders and craters. In contrast, the 9 m tilts do not resolve these variations. Instead, the 9 m tilts are affected by the curvature and long-wavelength character of the impact site DTM, which largely reflects the curvature of the global model. The curvature of the global model at long wavelengths, in turn, largely remains latched to the starter shape (e.g., Figure 18). In the 0.9 m tilt radius maps, the reconstructed impact site DTMs have a muted range of tilts

compared to the truth maps. This difference indicates that rock heights and crater depths are smoothed, as expected from SPC with far-from-optimal images (Barnouin et al. 2020). The broad patterns are similar, but with a narrower dynamic range. In the 9 m tilt maps, the reconstructed impact site DTMs also span a more muted range than in the truth impact site DTMs.

Histograms of the mean tilt distributions quantify these similarities and differences. Figures 23 and 24 show histograms of the tilt distributions for the maps shown in Figure 22. Both the mean and median for the truth versus reconstructed impact site DTMs show good agreement for both the 0.9 and 9 m tilt radii, with differences in the means of the truth and reconstructed tilts $\leq 7^\circ$. The mean of the reconstructed tilts is larger than the truth tilts for the Itokawa_DRACO, Itokawa_DRACO+LEIA, and Bennu_ideal cases. The reverse is true for the Bennu_errors case. The histograms for the 0.9 m tilts attest that, at that length scale, the range of tilts in the reconstructed impact site DTMs is muted compared to truth, as evidenced by the smaller range of tilt values. However, at the longer-baseline 9 m tilts, the reconstructed impact site DTMs in some cases actually have a larger range of tilts than the truth impact site DTMs. The smoothing at short length scales is expected, as noted previously, whereas the differences at longer length scales is driven by the latching of topography to the starter shape. In both cases, the shapes of the distributions in the reconstructed and truth models share key similarities, such as the bimodal distribution of tilts in the test with Itokawa.

Figure 25 shows the mean tilt with a 0.9 m tilt radius for just the facets inside the yellow circle (i.e., at the impact site of the DART spacecraft core). This is the area that will have the strongest effect on the normal vector to the DART impact. Once again, the measures of central tendency are within 7° for both the reconstructed and truth impact site DTMs in this

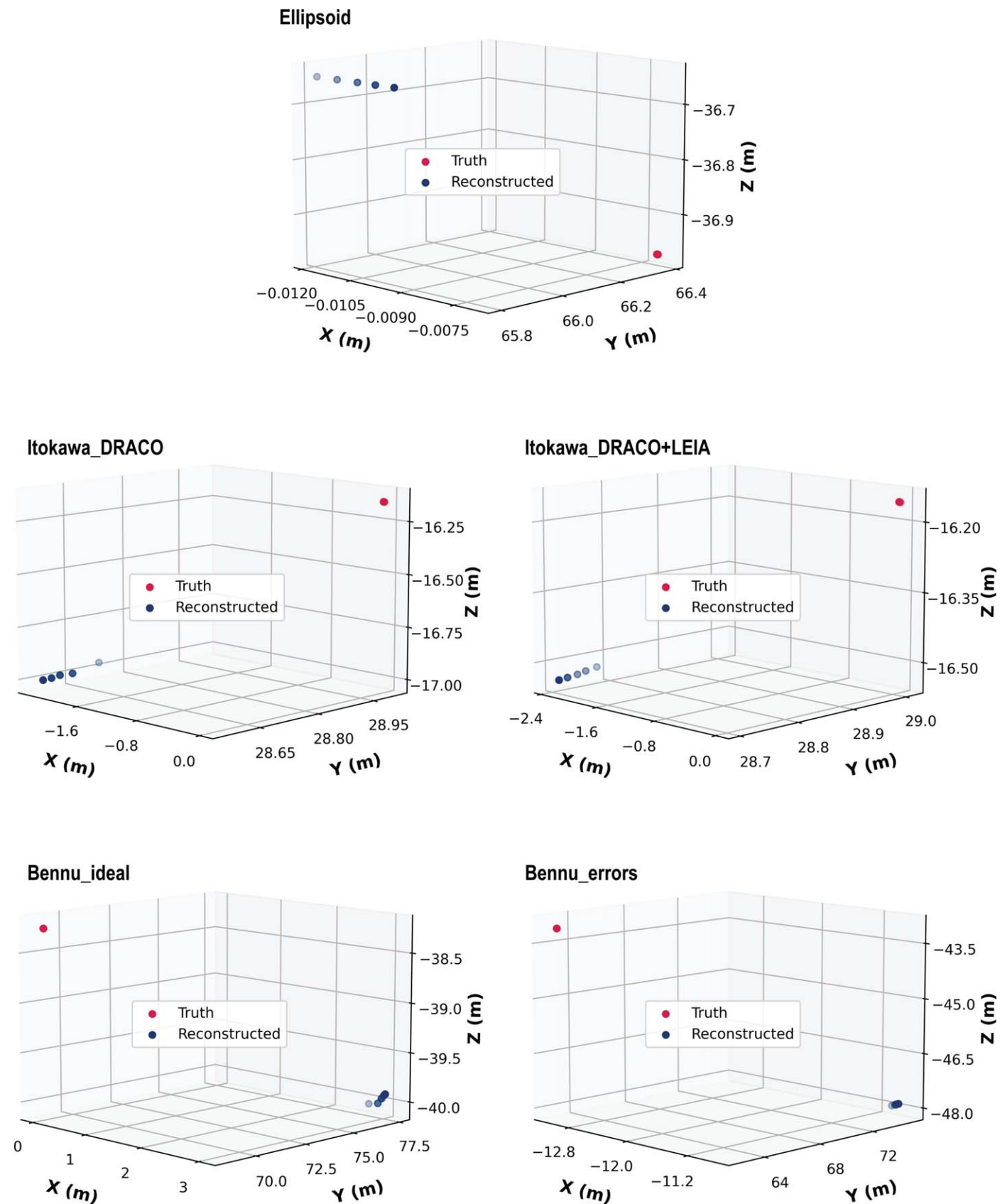


Figure 20. Location of the truth and reconstructed impact sites for each of the tests reported in this paper. The absolute location of the impact in 3D space is up to a few meters off from where it should be in the truth model, but that offset is small enough to not meaningfully affect the outcome of the DART experiment. The axes scales are different for each panel. Each blue dot corresponds to the solution for a given image in the reconstructed shape model. The reconstructed impact site is the average of the locations in the last five images.

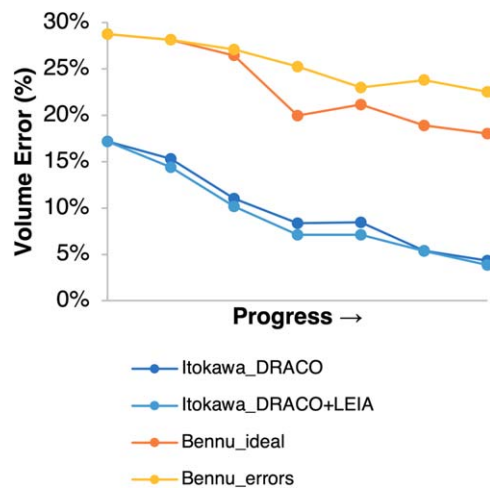


Figure 21. Volume error as function of shape model processing. The volume error decreases through the shape modeling process. Progress refers to the steps shown in Figure 2. From left to right, the dots correspond to the starting triaxial ellipsoid, the limb-based shape, the 60 cm maplet shape, the 25 cm maplet shape, the 10 cm maplet shape, the reflected and trimmed shape, and the final shape.

region. The shapes of the distributions are similar for the Itokawa cases (skewness of the same sign, similar kurtosis values), but differ in the Bennu cases (opposite skewness between truth and reconstructed, different kurtosis values).

The DART spacecraft core will contact and couple with an extended area on the surface of Dimorphos, not with a single point. So, it is the average mean tilt within the area contacted by the DART spacecraft that matters most. Table 7 summarizes the differences between the average mean tilts for all tests. The means (and medians) agree in all cases to within 7° . Errors of $\leq 7^\circ$ in impact angle would become important to interpretation of the DART impact in the event of an impact angle $< 30^\circ$ (as measured from the horizontal). The difference between a 30° and 23° impact may be meaningful in this case. Above that point, $\leq 7^\circ$ errors in impact angle would not be expected to meaningfully affect the direction of the momentum vector because the difference between a 60° and 53° (or 67°) impact are not as pronounced as they are for more oblique impact angles.

Although the mean tilt averaged over the maximum envelope of the DART spacecraft is what sets the impact angle, the direction of the momentum vector is also affected by the direction of the tilt because it affects the direction of the ejecta. Errors in tilt direction (e.g., the tilt is oriented more toward Didymos or more away from Didymos) would not affect the numerical impact models because such errors do not affect impact angle. However, they inform ejecta simulations (e.g., Schwartz et al. 2016; Yu et al. 2017; Larson & Sarid 2021) and could affect the two-body dynamics (e.g., Agrusa et al. 2021). Therefore, we also compared the tilt directions in the truth versus reconstructed models.

Figure 26 shows the distribution of tilt directions for the 0.9 m tilt radius. As with the mean tilt at this length scale, the reconstructed impact site DTM has a narrower range of tilt directions than the truth impact site DTM. The average and median mean tilt directions between truth and reconstructed are very similar for the Itokawa tests, but differ by up to 31° for the Bennu tests. This difference occurs because the impact site on Itokawa is on the wall of a crater that is a few times larger than

the maximum envelope of the DART spacecraft. But the impact site for Bennu_ideal is nestled between boulders that are comparable to or smaller than the size of the maximum envelope, and the tilt directions change rapidly around the boulders. Those boulders are not well represented in the reconstructed impact site DTM, which is too smooth. This smoothness contributes to the larger error in mean tilt direction. The Bennu_errors impact site is near the rim of a small crater that is not well represented in the reconstructed model, which contributes to the errors in tilt direction. Figures 27–29 show histograms of the distributions of mean tilt direction, and Table 8 summarizes the difference in average mean tilt direction between the truth and reconstructed impact site DTMs for the Itokawa and Bennu tests. Taken together, the results indicate that the *direction* of the normal vector to the shape model from the DART spacecraft will have larger uncertainties than the impact angle itself.

5.7. Local Height Differences

In the final comparison between the truth and reconstructed impact site DTMs, we identified common features in the truth and reconstructed models and then found the optimal translation and rotation to align those features. We then computed the residual between the two. This assessment provides a measure of how well the reconstructed models reproduce the local heights of features, such as boulders. Table 9 summarizes the results. The heights of features are reduced in the reconstructed DTMs, as expected. The errors are on the order to 20–40 cm, depending on the test.

6. Discussion

6.1. Effects of Assumed Truth Shape Model

Currently, the best information we have about the shape of Dimorphos comes from light-curve axial ratios, and that will remain the best-available information until DRACO resolves Dimorphos just minutes before impact. This fact is the motivation for using three different truth shape models in our tests. Here we discuss how these differences in shape affect impact site identification, volume error, and tilts near the impact site.

Impact site identification. Our ability to identify the pixel/line location of the impact site in the final DRACO image does not vary meaningfully with the truth shape. In all cases, we identify the impact site with an accuracy < 2 pixels or $\sim < 20$ cm (Table 5; Figure 19), which gives us confidence that we will know whether DART hit a block, boulder, smooth area, etc., regardless of what Dimorphos looks like, given the 2.5 m maximum envelope of the spacecraft core. The offsets between the truth and reconstructed impact sites in 3D space into and out of the image plane (Table 6; Figure 20), however, do appear to depend on shape. The differences are not so much about the specific shape, but about how far the starter shape is from the truth shape at the impact point at the beginning of the test because the fine-scale topography latches onto the starter shape. The larger offsets occur in the Bennu tests, which are the tests where the starter shape lies farthest from the truth shape. However, as noted in Section 5, these offsets in 3D space amount to no more than 8% of the volume-equivalent diameter of Dimorphos and will not meaningfully affect the outcome of any DART impact simulations following the impact, unless the impact occurs very close to the limb.

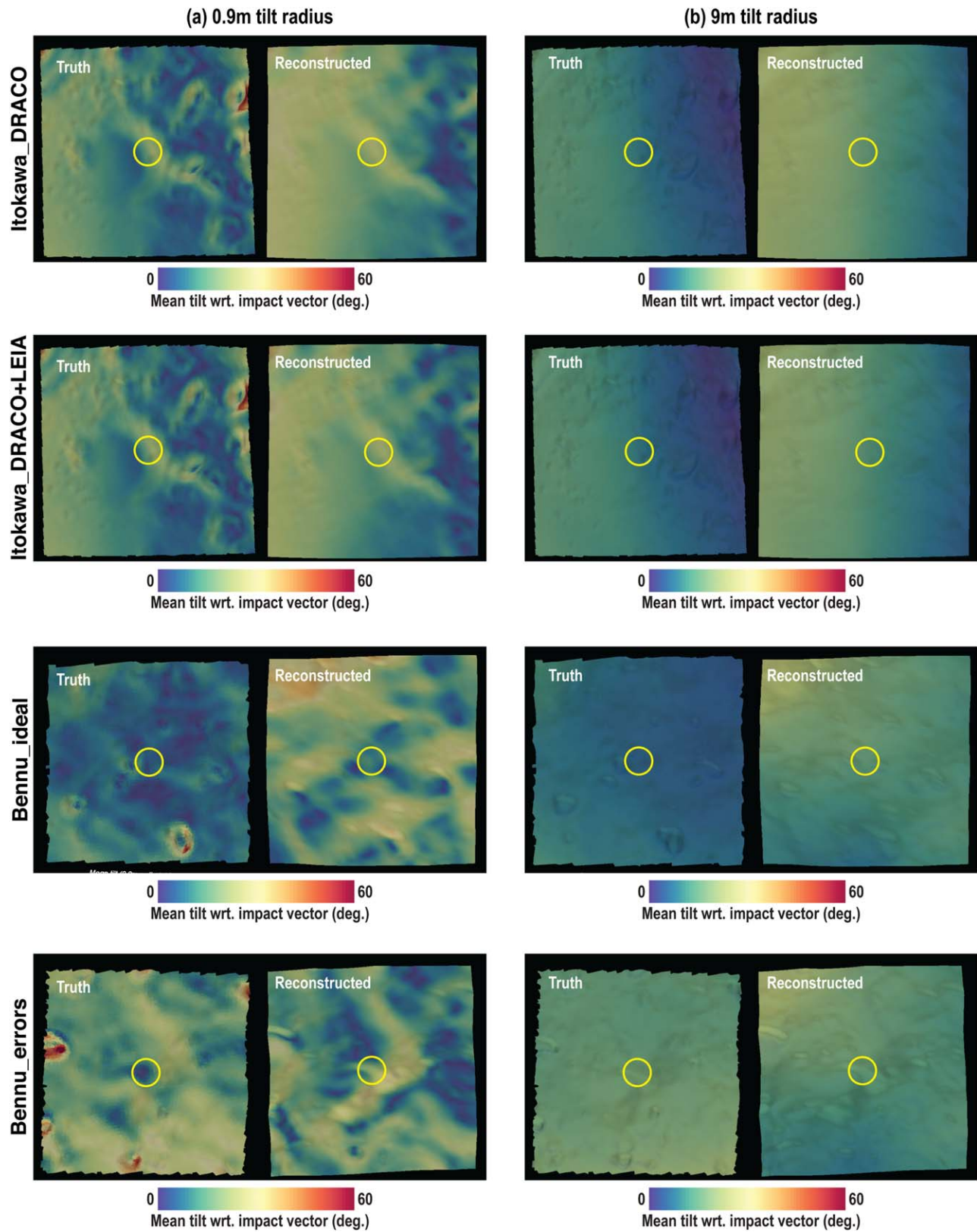


Figure 22. Mean tilt of facets in the impact site DTM. Tilts are computed with respect to the spacecraft impact vector, thereby providing information about the relative impact angle between DART and the asteroid. The figure shows tilts at two different radii: (a) the 0.9 m tilt radius provides information on tilts at the length scale of the core of the DART spacecraft; (b) the 9 m tilt radius provides information about tilts at the length scale of the DART spacecraft with solar arrays extended. All maps use a common color scale to facilitate comparisons between the 0.9 and 9 m tilt maps. The yellow circle is 2.5 m in diameter, the size of the maximum envelope of the DART spacecraft core. The impact site DTMs are 18.9 m on a side; the extended solar arrays would span almost the entire width of the impact site DTM.

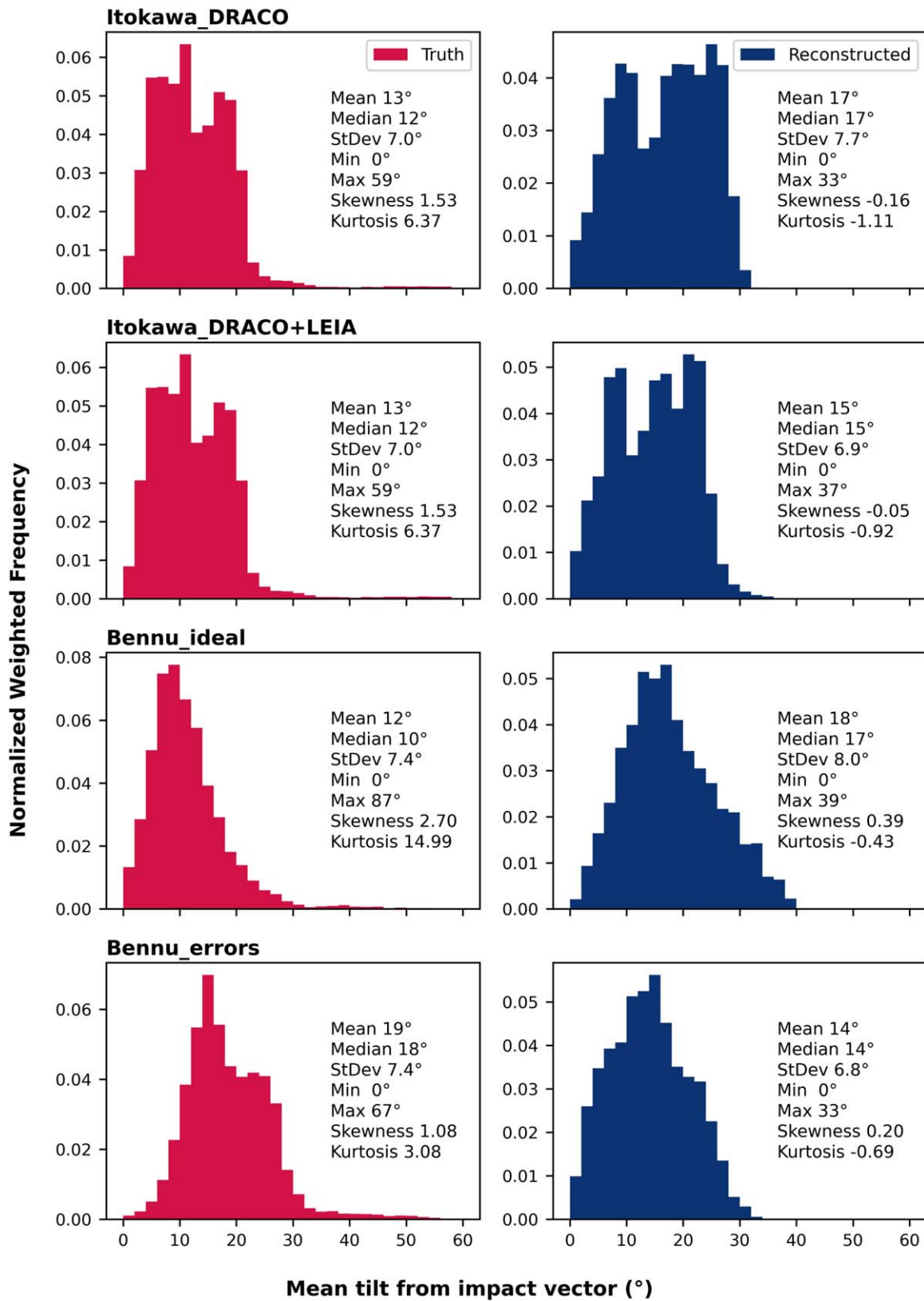


Figure 23. Mean tilts across the impact site DTMs with respect to the spacecraft impact vector, with a tilt radius of 0.9 m. The left column (red) plots the distributions for the truth model. The blue column (right) plots the distributions for the reconstructed impact site DTMs. The difference in the mean and median tilts between the truth and reconstructed cases is between 2° and 7°, depending on the case.

Volume. The Bennu tests have larger volume errors than the Itokawa tests (Table 7; Figure 21). These differences tie to the magnitude of the errors in the starter shape: the larger the

volume error in the starter shape, the larger the volume error in the final shape. A starter shape that sticks out too far in some areas and not enough in others leads overall to a better volume

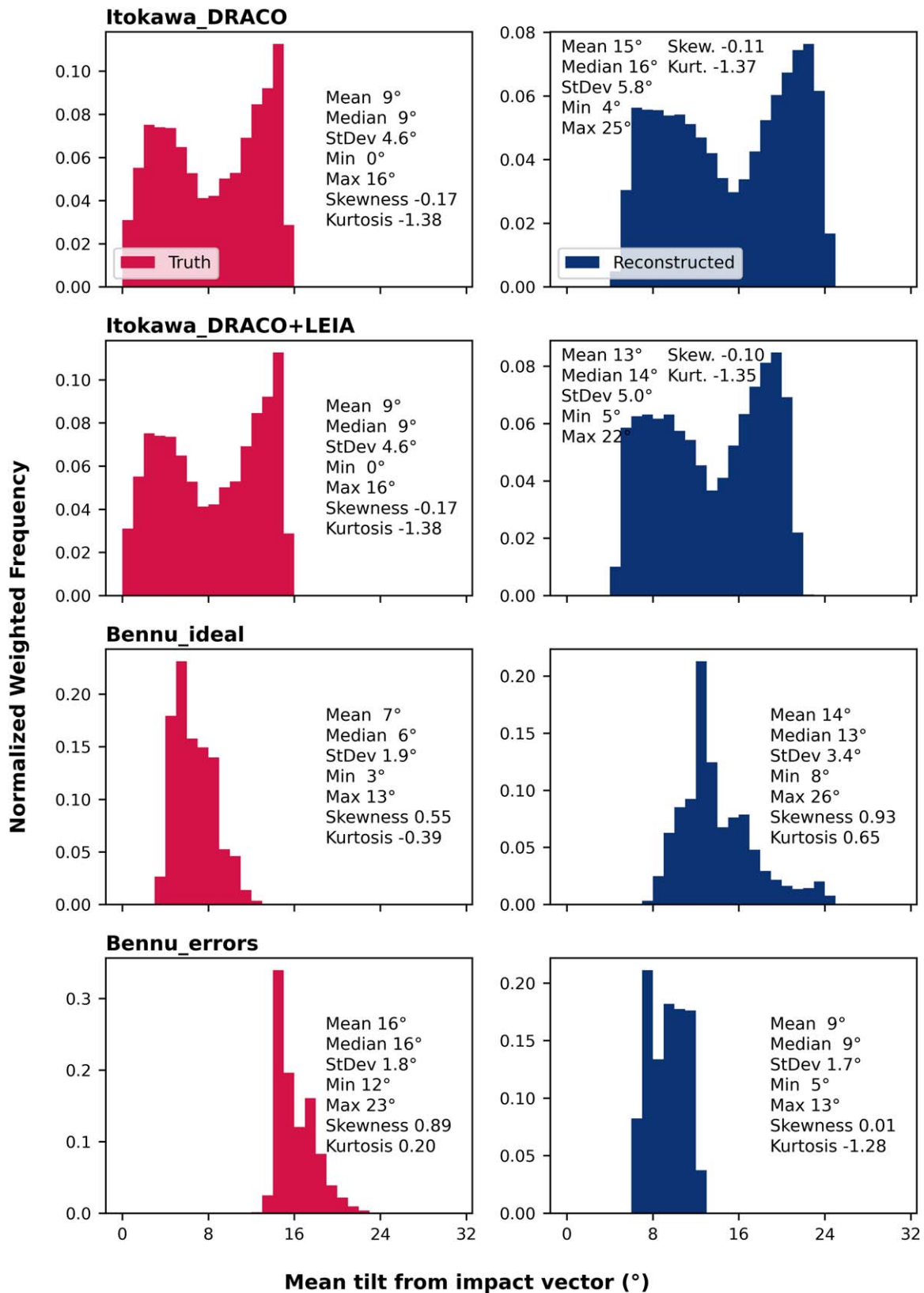


Figure 24. Mean tilts across the impact site DTMs with respect to the spacecraft impact vector, with a tilt radius of 9 m. The left column (red) plots the distributions for the truth model. The blue column (right) plots the distributions for the reconstructed impact site DTMs. The difference in the mean and median tilts between the truth and reconstructed cases is between 4° and 7°, depending on the case.

estimate than a starter shape that is too large almost everywhere. It is easier to have such a starter shape for a body that is concave in some areas and convex in others, like

Itokawa, than it is on a diamond-shaped body like Bennu. When images of Dimorphos start streaming in, drawing analogies between Dimorphos and other asteroids will help

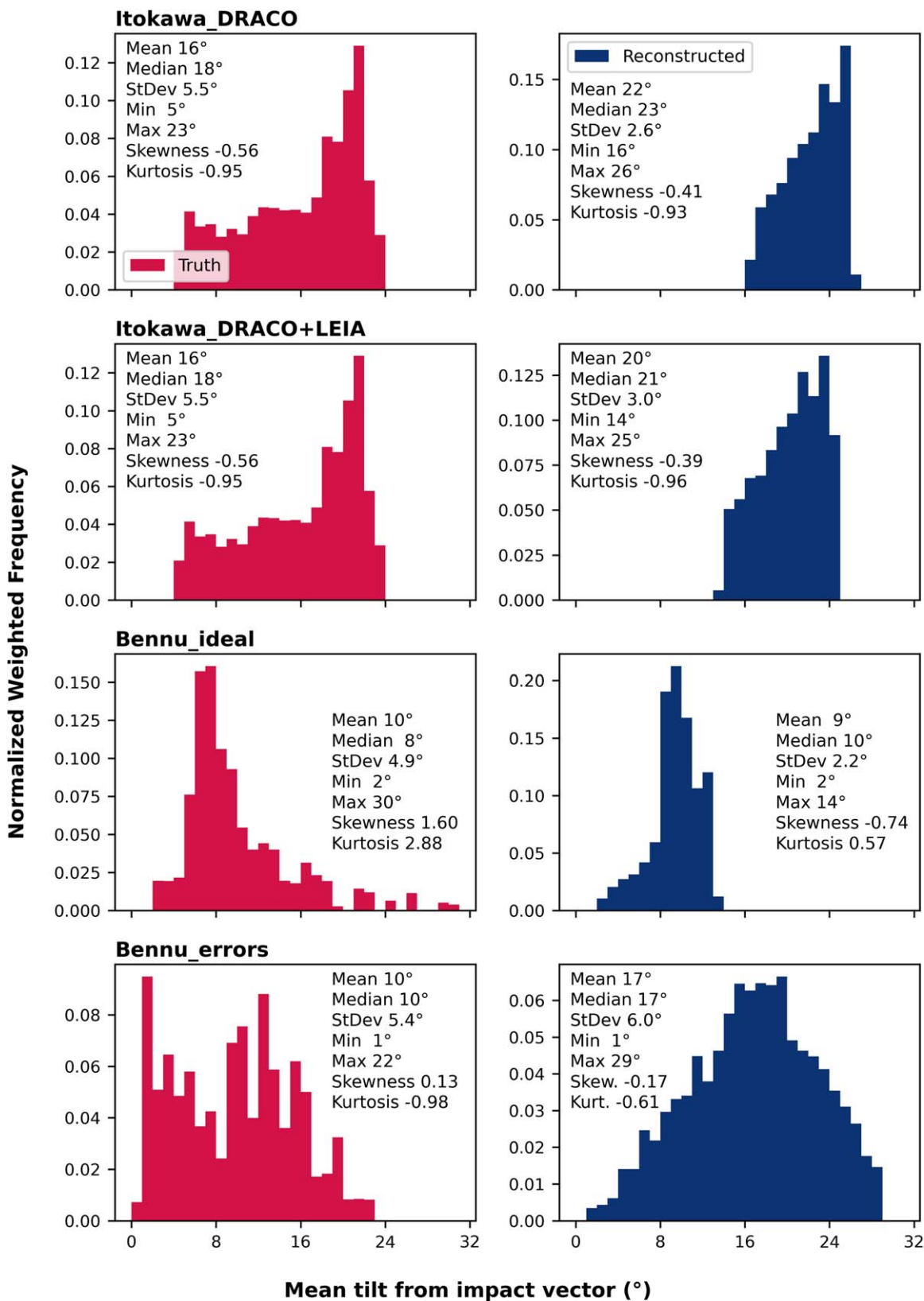


Figure 25. Mean tilts across the impact site DTMs, focusing only on the region of the DTM within the spacecraft core maximum envelope (2.5 m), with respect to the spacecraft impact vector, with a tilt radius of 9 m. The left column (red) plots the distributions for the truth model. The blue column (right) plots the distributions for the reconstructed. The difference in the mean and median tilts between the truth and reconstructed cases is between 1° and 7°, depending on the case.

Table 7
Volume Assessments from DART Shape Modeling Tests

Test	Starting Model Error (Vol. %)	Final Model Error (Vol. %)	Improvement in Volume Error vs. Starter Shape (%)	Uncertainty in β (%) ^a
Ellipsoid	−38	−2	95	25
Itokawa_DRACO	17	4	76	25
Itokawa_DRACO+LEIA	17	4	76	25
Bennu_ideal	29	18	38	31
Bennu_errors	29	23	21	34

Note.

^a Beta uncertainty assumes a 25% density uncertainty.

identify a good starter shape model. In the DART scenario—with redundant images of only part of the illuminated half of the body—the starter shape exerts significantly more sway than it does for bodies with global coverage or even regional coverage from a variety of viewing geometries. In all cases, however, the shape modeling process reduced the volume error by 20%–95%, depending on the test.

Impact site tilts. In all cases, the average mean tilt across the impact site DTM is $\leq 7^\circ$ (Table 10; Figures 22–25). The Itokawa tests have smaller discrepancies between the truth and reconstructed tilts than the Bennu tests, particularly for the 0.9 tilt radius. At that tilt radius, the differences are likely due more to the differences in the local topography than the bulk shape. Itokawa is smoother near the impact site in the Itokawa tests than Bennu is near the impact sites in both Bennu_errors and Bennu_ideal. These same factors likely also explain the larger tilt direction errors in the Bennu cases (Table 8; Figures 26–29). The reconstructed topography does not capture the extremes in tilts in either case, and the heights of boulders on Bennu are suppressed and their edges smoothed. Smoothing of steep slopes is a known consequence of SPC (Barnouin et al. 2020), but the effect is severely exacerbated for DART because of the lack of stereo (LEIA images are too coarse to contribute to the fine-scale topography) and single lighting direction. If Dimorphos is as rugged as Bennu, we will underestimate the rock heights and tilts, which will lead to errors in the average tilt across the impact site that are closer to 7° than to the $2\text{--}4^\circ$ seen in the Itokawa tests. At the longer 9 m tilt radius, the differences are less pronounced between the Itokawa and Bennu tests, likely because differences in the long-wavelength shape—which are challenging to capture regardless of shape because so little of the body is actually seen—play more of a role. The ruggedness of the terrain (smooth versus boulder-rich) will give a sense for whether the tilt errors are likely to be more like those from the Itokawa tests or more like those from the Bennu tests. However, in all cases the tilt errors are small enough that they will not meaningfully affect the magnitude of the DART impact unless the impact is highly oblique.

6.2. Effects of LEIA Images

As noted previously, the LEIA images are much coarser than the DRACO images and will only be incorporated into the coarsest set of landmarks. This limits the extent to which the stereo from LEIA helps to pull the topography into the correct 3D location because the stereo information from LEIA cannot directly influence the locations of the 25 and 10 cm maplets. However, the limbs provided by LEIA provide useful information that helps to improve the bulk shape (Figure 16).

The caveat is that the simulated LEIA images used in these tests did not include ejecta, but in reality the LEIA images will probably contain ejecta, which may further limit their usefulness, depending on the quantity and distribution of ejecta. The baseline plan is to rely on DRACO images alone.

Impact site identification. The LEIA images do not meaningfully improve impact site identification in either pixel/line space in the final DRACO image or in 3D space (Figure 19; Tables 5 and 6). LEIA images would not be expected to have any effect on the pixel/line accuracy, since those measurements are done with respect to the final DRACO image. The fact that the images did not meaningfully change the offset in 3D space likely stems from the fact that even with LEIA we see only a fraction of the lit portion of the body, much of the final shape remains at the mercy of the starter shape, and the images are coarse enough that they affect only the coarsest maplets.

Volume. The LEIA images did not improve the volume estimate (Table 7). However, they did bring the bulk shape closer to the truth shape (Figure 16).

Impact site tilts. The differences in the truth versus reconstructed mean tilt and mean tilt directions for the DRACO+LEIA versus DRACO-only tests are small enough to doubt whether they are actually significant. The average mean tilt difference is slightly smaller in the test with LEIA versus the test without LEIA, but the truth versus reconstructed mean difference is within 2° for both tests. The mean tilts cover a slightly larger range in the test with LEIA (Table 10; Figures 22–25). The differences in error in mean tilt direction between the two tests are within a couple of degrees of each other. It is not surprising that the LEIA images do not have a noticeable effect on the tilts, especially in the 0.9 m tilt radius because the finer-scale topography is generated from DRACO images only. The LEIA images are simply too coarse to contribute to it.

In summary, while the LEIA images help to improve the bulk shape of the asteroid (Figure 16), they do not meaningfully improve knowledge of the impact site location, volume, and impact site tilts. That is good news, in one view, because it means that the quality of these three pieces of information does not depend on the availability of LEIA images. It also negates the need to undertake shape modeling tests with LEIA images that include ejecta.

6.3. Effects of Uncertainties in Spacecraft Position and Camera Pointing

In comparing the two Bennu cases (Bennu_ideal without errors and Bennu_errors with errors), it is essential to keep in mind that the two tests have different impact sites and “zoom in” on different parts of Bennu (Figures 6 and 19). Importantly,

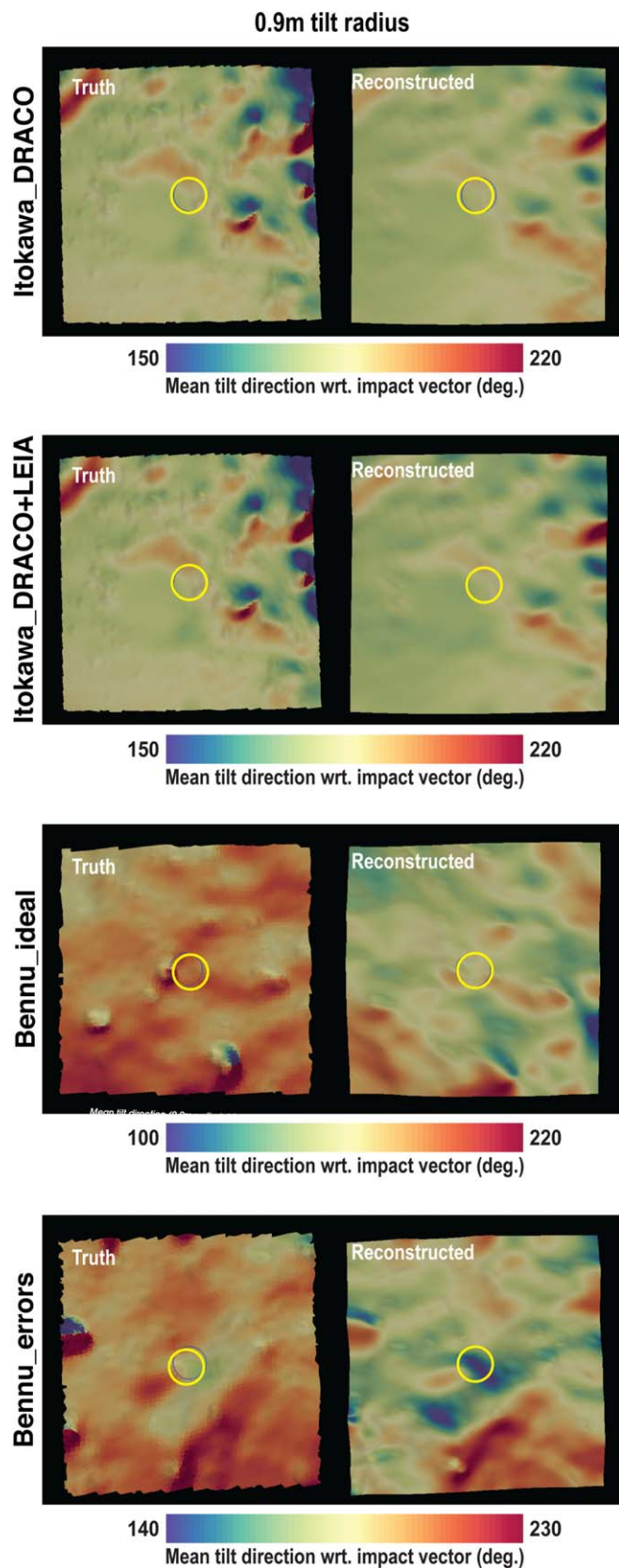


Figure 26. Mean tilt directions of facets in the impact site DTMs. Tilt directions are computed with respect to the spacecraft impact vector, thereby providing information about the relative impact angle between DART and the asteroid. The figure shows tilts at two different radii. The 0.9 m tilt radius provides information on tilts at the length scale of the core of the DART spacecraft. The tilt direction is the direction projected on a clock, with a 0° tilt direction pointing to the north pole of the asteroid.

the impact site in the *Bennu_errors* case is about 13 m closer to the terminator than in the *Bennu_ideal* case.

Impact site identification. In both cases, we identify the impact site within <2 pixels in the final DRACO image (Figure 19; Table 5). That the two *Bennu* tests yield similar results for this parameter indicates that SPC is successfully correcting the errors in spacecraft position and camera pointing. The two tests also have similar rms residuals per maplet and sigma values (Figure 12; Table 4), which is another line of evidence that SPC successfully corrected for the errors in spacecraft position and camera pointing. However, the offset between the truth and reconstructed impact sites for the error case in 3D space is larger than the corresponding offset for the ideal case. This difference occurs because the terrain toward the terminator is built up higher in the error case than in the ideal case, and the impact site in the error case is nearer the terminator than in the ideal case. Because DRACO provides only one view with one lighting condition, areas near the terminator are increasingly hard to model because the topography in every shadowed pixel is poorly constrained.

Volume. The error case has a larger volume error than the ideal case (Figure 21; Table 7). However, this is not so much due to the errors in spacecraft position and camera pointing (which SPC corrects for effectively, as evidenced by the similar SPC metrics). Instead, this difference in volume stems largely from a choice made by the shape model producer. The modeler trimmed much more severely in the ideal shape than in the error shape (note the large decrease in the dark orange data series in Figure 21, versus the smoother decrease in the light orange data series). Shape modeling is, in part, an art, particularly when most of the body is never seen. Nevertheless, for both cases, the shape modeling process decreased the volume error.

Impact site tilts. The differences between both the average mean tilt in the truth and reconstructed impact site DTMs are similar in magnitude for both the ideal and error *Bennu* tests but different in sign. In the ideal case, the reconstructed tilts tend to be too steep on average, whereas in the error case they are too small on average. The difference in sign is not directly attributable to the errors in spacecraft position and camera pointing because the spacecraft in the ideal and error cases collided with *Bennu* in two different places. The error case for *Bennu* has a smaller error in the average mean tilt direction than the ideal case. This result stems from the fact that the *Bennu_ideal* case impacted among some boulders, which are not captured well in the reconstructed impact site DTM, leading to $\sim 30^\circ$ errors in the average mean tilt direction. The *Bennu_ideal* impact is smoother than the *Bennu_errors* impact site, and the *Itokawa_DRACO* and *Itokawa_DRACO+LEIA* impact sites (which are the same) are smoother still. The errors between the average mean tilt direction in the truth and reconstructed models tracks with that trend. The ruggedness of the local topography appears to drive the errors in mean tilt direction, not the errors in spacecraft position and camera pointing in the images.

6.4. Lessons Learned

The shape modeling tests reported here illustrate the challenges of modeling the shape of an asteroid when less than half of the body is both visible to the camera and illuminated, the highest-resolution images possess essentially no stereo information, and the sole data set that could provide some stereo is so coarse in comparison to the

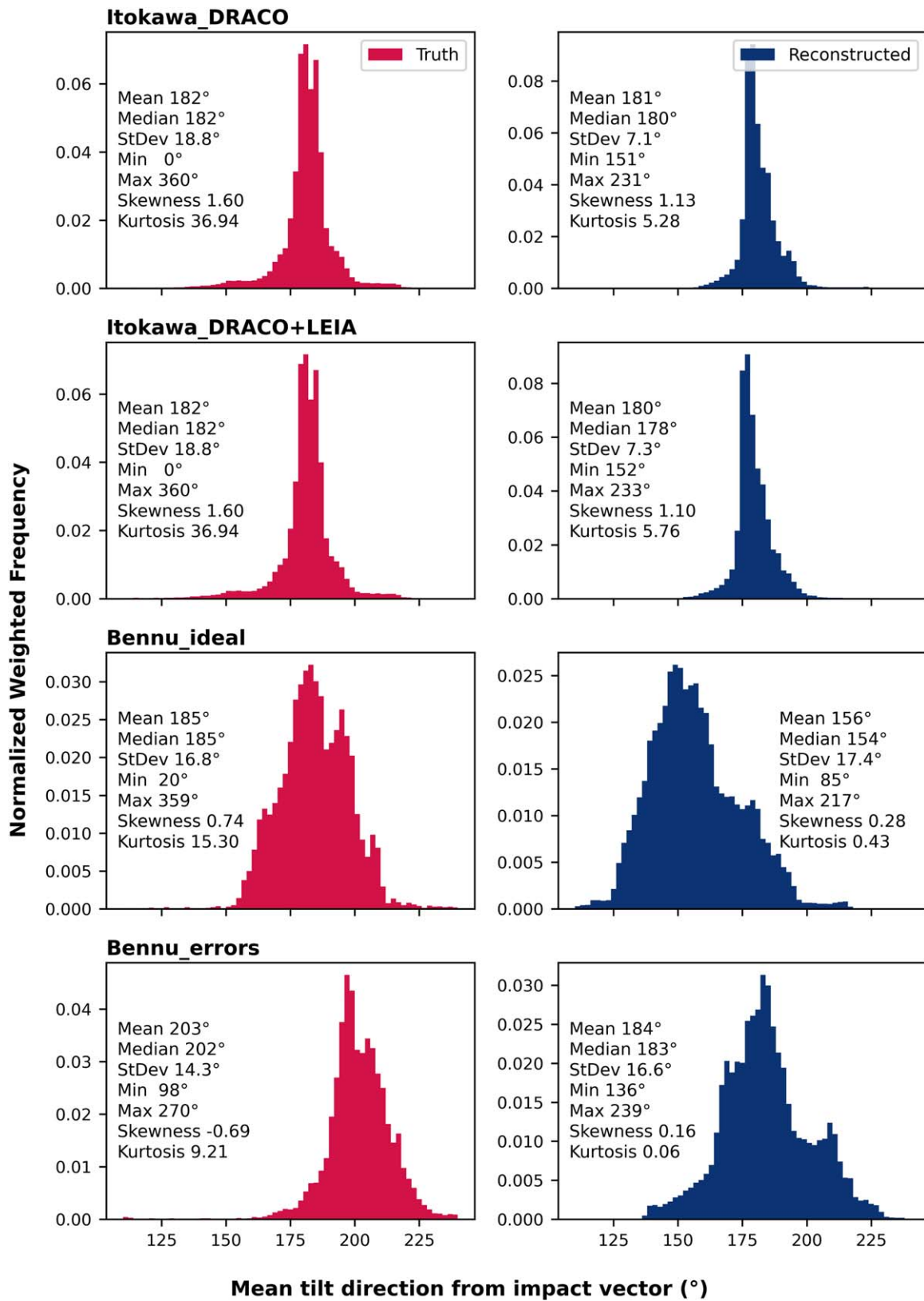


Figure 27. Mean tilt directions across the impact site DTMs with respect to the spacecraft impact vector, with a tilt radius of 0.9 m. The left column (red) plots the distributions for the truth model. The blue column (right) plots the distributions for the reconstructed impact site DTMs. The difference in the mean and median tilt directions between the truth and reconstructed cases is between 1° and 31°, depending on the case.

high-resolution images that they are difficult to tie together into maplets. Despite these challenges, the tests reported here show that we will be able to reliably identify the impact site

of the DART spacecraft, significantly improve the estimated volume of Dimorphos versus a triaxial ellipsoid based on light curves, and determine the tilts at the impact site well

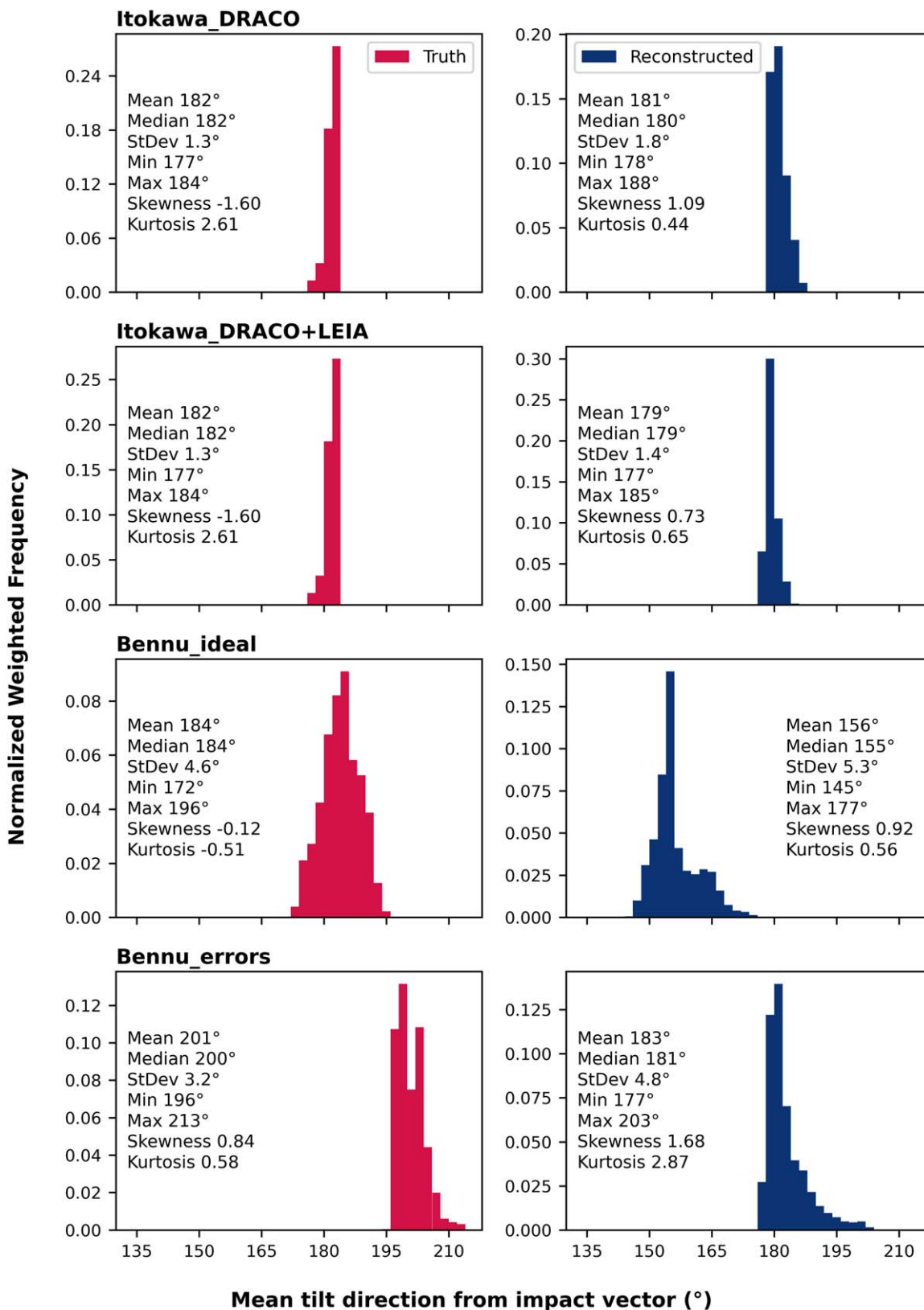


Figure 28. Mean tilt directions across the impact site DTMs with respect to the spacecraft impact vector, with a tilt radius of 9 m. The left column (red) plots the distributions for the truth model. The blue column (right) plots the distributions for the reconstructed impact site DTMs. The difference in the mean and median tilt directions between the truth and reconstructed cases is between 1° and 29°, depending on the case.

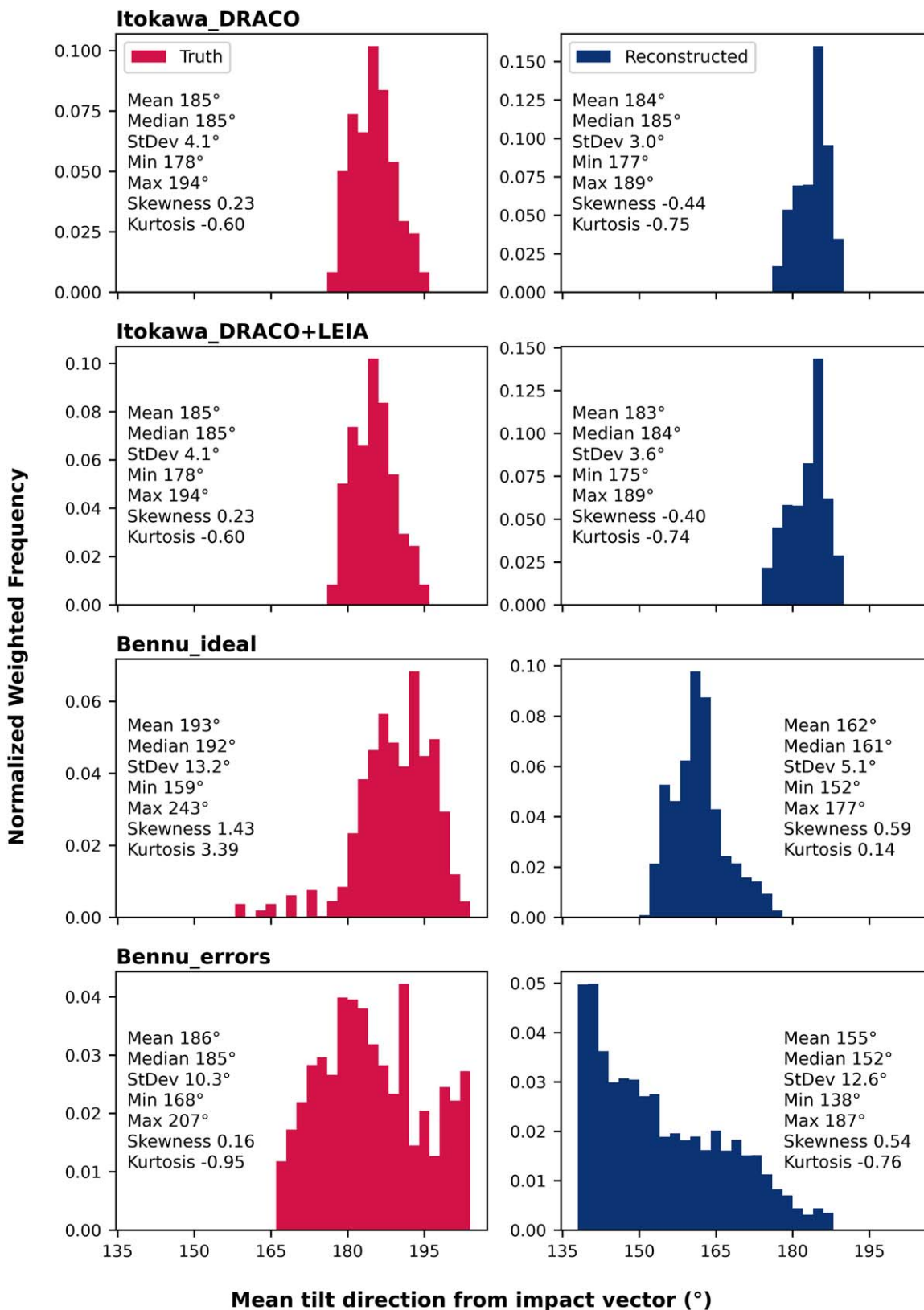


Figure 29. Mean tilt directions across the impact site DTMs, isolating just the max envelope of the DART spacecraft core, with respect to the spacecraft impact vector, with a tilt radius of 0.9 m. The left column (red) plots the distributions for the truth model. The blue column (right) plots the distributions for the reconstructed impact site DTMs. The difference in the mean and median tilt directions between the truth and reconstructed cases is between 1° and 33°, depending on the case.

Table 8
Mean Tilt Direction Assessments from DART Shape Modeling Tests^a

Test	Truth: Avg. Mean Tilt Direction			Reconstructed: Avg. Mean Tilt Direction			Difference		
	0.9 m Tilt Radius	9 m Tilt Radius	Impact site; 0.9 m Tilt Radius	0.9 m Tilt Radius	9 m Tilt Radius	Impact site; 0.9 m Tilt Radius	0.9 m Tilt Radius	9 m Tilt Radius	Impact site; 0.9 m Tilt Radius
Itokawa_DRACO	182°	182°	185°	181°	181°	184°	-1°	-1°	-1°
Itokawa_DRACO +LEIA	182°	182°	185°	180°	179°	183°	-2°	-3°	-2°
Bennu_ideal	185°	184°	193°	156°	156°	162°	-29°	-28°	-31°
Bennu_errors	203°	201°	186°	184°	183°	155°	-19°	-18°	-31°

Note.

^a ideal1_draco is not shown because no maplets were generated in that test; the tilt directions in the truth and reconstructed models are the same because they are both triaxial ellipsoids with identical axial ratios.

Table 9
Height Differences between Truth and Reconstructed Impact Site DTMs

Test	Mean Residual (m)	Median Residual (m)	Standard Deviation (m)
Itokawa_DRACO	0.06	0.05	0.28
Itokawa_DRACO +LEIA	0.01	0.06	0.23
Bennu_ideal	0.12	0.17	0.27
Bennu_errors	-0.01	0.01	0.41

enough to provide a reliable measure of the impact angle of the DART spacecraft.

As a result of these tests, we learned the following. These lessons learned are helpful not only to DART but also to future planetary defense or small-bodies missions that will fly by (rather than rendezvous with) small bodies. However, some of these are more relevant to DART because of the severely limited images inherent to this mission:

1. Without robust stereo in images of similar resolution, the starter shape exerts considerable sway over the final shape model. Fine-scale topography can be generated by SPC that is a good match to features in the images, but the absolute position of those features in 3D space into and out of the image plane is poorly constrained. This emphasizes the need to have the best possible starting shape. Comparisons between the location of the terminator in images versus the shape can improve the choice of starter model. Light-curve axial ratios also provide important constraints. In flight, we may use a low-resolution shape of an analogous asteroid as a starting shape; we also plan to use the reconstructed shape models of Dimorphos and Didymos to generate simulated light curves and assess how well they match the observed light curves. This comparison will provide an additional measure of shape model quality.
2. Limbs provide crucial constraints on the bulk shape and sculpt the shape model to match the images, even if they do not improve the volume estimate or meaningfully change the quality of information about the impact site. The use of limb vectors and limb-only maplets to improve the shape was essential to match the portions of images that were too high emission to support reasonable maplets. Due to the relatively coarse resolution of the LEIA images,

some of the limb-search parameters in SPC had to be relaxed compared to the baseline values that might be appropriate for a rendezvous mission in order to incorporate limb information into the topography of standard maplets. The scatter of limb points provides information about how well the limb is represented in the model, particularly in the direction perpendicular to the image.

3. Information about what is *not* visible and illuminated in the images is an important constraint on the shape model in areas that are not imaged by DRACO or LEIA. We do not know what the shape *is* in those areas, but we know what the shape *is not* in those areas. Trimming the shape model to ensure that areas that are not visible and illuminated in the images are also not visible and illuminated in the rendered shape model provides an important constraint to the final shape in the unseen areas.
4. The reliability of the model degrades as you move toward the terminator. This is not surprising in the case of DART, where areas that are in shadow in one DRACO image are in shadow in all DRACO images, and SPC has no image data to work with. However, mismatches between the terminator in images versus the rendered shape model are one of the only constraints on the shape into and out of the image plane. Terminator data will be used to constrain the broader-scale curvature of a starter model. A starter model that better matches the terminator in the image should lessen the degradation in topography as you approach the terminator.
5. Internal SPC metrics are not as reliable with far-from-optimal images as they are with images optimized for SPC. The formal uncertainty metric breaks down without meaningful stereo, and the vertex sigma and rms residuals per maplet indicate much smaller uncertainties than those revealed by comparisons with the truth shapes. The SPC metrics correctly indicate good precision, but do not capture the overall errors in 3D space, which are largely into and out of the plane of DRACO images.

Several of these lessons can be leveraged for future shape modeling efforts from missions that rely on flybys. Images from a well-designed flyby mission would provide reasonable stereo, which would lessen the influence of the starter shape on the final model. In a flyby mission, the stereo in the images may mitigate the issues DART encounters in modeling terrain near the terminator, although some areas would always be in

Table 10
Mean Tilt Assessments from DART Shape Modeling Tests^a

Test	Truth: Avg. Mean Tilt			Reconstructed: Avg. Mean Tilt			Difference		
	0.9 m Tilt Radius	9 m Tilt Radius	Impact site; 0.9 m Tilt Radius	0.9 m Tilt Radius	9 m Tilt Radius	Impact site; 0.9 m Tilt Radius	0.9 m Tilt Radius	9 m Tilt Radius	Impact site; 0.9 m Tilt Radius
Itokawa_DRACO	13°	9°	16°	17°	15°	22°	4°	6°	6°
Itokawa_DRACO +LEIA	13°	9°	16°	15°	13°	20°	2°	4°	4°
Bennu_ideal	12°	7°	10°	18°	14°	9°	6°	7°	-1°
Bennu_errors	19°	16°	10°	14°	9°	17°	-5°	-7°	7°

Note.

^a ideal1_draco is not shown because no maplets were generated in that test; the curvatures of the truth and reconstructed models are the same because they are both triaxial ellipsoids with identical axial ratios.

shadow. A flyby mission would provide more limbs than DRACO will, which would help better constrain the bulk shape. Additional views of the body from a flyby would allow the trimming technique to be used in more places.

7. Conclusions

Shape modeling efforts will improve interpretations of the DART impact (Rivkin et al. 2021). The volume of the global shape model will be used to determine the best-available estimate of the mass of Dimorphos until the ESA’s Hera mission’s rendezvous with Didymos (Michel et al. 2022). Coregistered images (a byproduct of the SPC shape modeling efforts) and knowledge of the spacecraft trajectory will be used to constrain the location of the impact site.

The DART mission will use SPC to build shape models of Dimorphos. The shape models will be built from images of Dimorphos acquired by the DRACO camera on DART during approach and, if available, additional lower-resolution images acquired by the LEIA camera on LICIACube that provide some stereo information. DART poses a stressing case for shape modeling, as most of the body is never seen because it is either in the dark or illuminated but not seen. In addition to limited spatial coverage, the images will have little to no stereo and minimal lighting variation. All of the resolved images useful for shape modeling will be collected in just a handful of minutes leading up to (and for LEIA only shortly after) impact.

The shape modeling tests done for DART indicate the following. We will know where DART hit in the final DRACO image with an accuracy of <2 pixels, or better than 20 cm. The error in asteroid volume will be <25%, but could be much lower. The mean tilt at the impact site will be known to within 7°. The range of tilts will be suppressed in the impact site DTM compared to reality. Errors up to ~30° may occur in the direction of the tilt.

The tests also show that the model quality will be limited by the limited images. The absolute positions of features in 3D space will be off by up to ~15 m. The heights of rocks will be muted, and the range of tilts will be too narrow. The fine-scale topography will largely be expressed as deviations from the surface of the starter shape. Once we see what Dimorphos looks like, we will be able to use what we learned from these tests to better understand how well we expect the Dimorphos model to perform and its likely strengths and weaknesses. In addition, once we know what Dimorphos looks like, we can use analogies with other asteroids, such as

Itokawa, Eros, Bennu, and to assess what we are likely to represent well in the shape model and what is likely to have larger errors.

Despite the limitations, these results show that we will know definitively whether DART hit a block, boulder, or smooth area because the uncertainty in the impact site location is only a few percent of the size of the spacecraft. We will know the volume well enough that uncertainty in the density of Dimorphos—which DART has no way to measure—will contribute equally to, if not more than, the uncertainty in the best estimate of the mass of Dimorphos. We will know the impact angle to within 7°, which is a small enough uncertainty as to not meaningfully affect the outcome of the DART impact, unless the impact is highly oblique. These results provide confidence that the DART team will be able to accurately interpret the results of the DART impact.

It is important to remember that in flight there is no truth model against which to compare; but, we have other means to assess model quality, including internal SPC metrics, qualitative comparisons to images, quantitative comparisons to images, such as the limb/terminator and feature assessments, light-curve data, and analogies with other small asteroids. Comparisons to images will provide critical information about how well the shape model matches a 2D image. In-flight information about the quality of the model into and out of the page will remain limited.

Ultimately, the Hera mission will rendezvous with Dimorphos and determine its mass and shape with the precision that can only be achieved by a rendezvous mission (Michel et al. 2022). Hera may observe a crater, a resurfaced region, a hemispheric disturbance, or even a global rearrangement depending on the structural and seismological properties of Dimorphos, which we do not know (Stickle et al. 2022, this focus issue). The global, image-based shape model from Hera will be compared to the DART model and images to identify areas of major change, that in turn can be related to the structural response and provide important constraints on numerical simulations of the impact and the asteroid’s deflection.

In the meantime, the global shape model and impact site DTM produced from the meager set of suitable DART images will provide humanity’s best information about the shape of the asteroid targeted by the world’s first planetary defense test mission. That we can do as well as we do is a testament to the power and versatility of SPC as a shape modeling technique.

This work was supported by the DART mission under NASA Contract 80MSFC20D0004. This work was supported by the Italian Space Agency (ASI) within the LICIACube project (ASI-INAF agreement AC n. 2019-31-HH.0). This work used the Small Body Mapping Tool (sbmt.jhuapl.edu). JMTR is funded by FEDER, Ministerio de Ciencia e Innovación and Agencia Estatal de Investigación of Spain. Erik Asphaug, Steve Schwartz, and Masatoshi Hirabayashi provided valuable comments on the manuscript.

ORCID iDs

R. Terik Daly  <https://orcid.org/0000-0002-1320-2985>
 Carolyn M. Ernst  <https://orcid.org/0000-0002-9434-7886>
 Olivier S. Barnouin  <https://orcid.org/0000-0002-3578-7750>
 Eric E. Palmer  <https://orcid.org/0000-0001-6755-8736>
 Angela M. Stickle  <https://orcid.org/0000-0002-7602-9120>
 Josep M. Trigo-Rodríguez  <https://orcid.org/0000-0001-8417-702X>
 Maurizio Pajola  <https://orcid.org/0000-0002-3144-1277>
 Simone Ieva  <https://orcid.org/0000-0001-8694-9038>
 Patrick Michel  <https://orcid.org/0000-0002-0884-1993>

References

- Agrusa, H. F., Gkolias, I., Tsiganis, K., et al. 2021, *Icar*, **370**, 114624
 Al Asad, M. M., Philpott, L. C., Johnson, C. L., et al. 2021, *PSJ*, **2**, 82
 Anderson, J. L. B., Schultz, P. H., & Heinecke, J. T. 2003, *JGRE*, **108**, E85094
 Barnouin, O. S., Daly, M. G., Palmer, E. E., et al. 2019, *NatGe*, **12**, 247
 Barnouin, O. S., Daly, M. G., Palmer, E. E., et al. 2020, *P&SS*, **180**, 104764
 Cheng, A. F., Michel, P., Jutzi, M., et al. 2016, *P&SS*, **121**, 27
 Cheng, A. F., Stickle, A. M., Fahnestock, E. G., et al. 2020, *Icar*, **352**, 113989
 Cheng, A. F., Weaver, H. A., Conard, S. J., et al. 2008, *SSRv*, **140**, 189
 Daly, M. G., Barnouin, O. S., Seabrook, J. A., et al. 2020, *SciA*, **6**, eabd3649
 de León, J., Licandro, J., Duffard, R., & Serra-Ricart, M. 2006, *AdSpR*, **37**, 178
 de León, J., Licandro, J., Serra-Ricart, M., Pinilla-Alonso, N., & Campins, H. 2010, *A&A*, **517**, A23
 DellaGiustina, D. N., Burke, K. N., Walsh, K. J., et al. 2020, *Sci*, **370**, eabc3660
 Dotto, E., Della Corte, V., Amoroso, M., et al. 2021, *P&SS*, **199**, 105185
 Ernst, C. M., Gaskell, R. W., Barnouin, O. S., & Daly, R. T. 2018, *LPSC*, **49**, 2769
 Ernst, C. M., Gaskell, R. W., Daly, R. T., Barnouin, O. S., & Thomas, P. C. 2019, *LPSC*, **50**, 2640
 Fang, J., & Margot, J.-L. 2012, *AJ*, **143**, 24
 Feldhacker, J. D., Sval, M. B., Jones, B. A., et al. 2017, *JGCD*, **40**, 2417
 Fletcher, Z. J., Ryan, K. J., Maas, B. J., et al. 2018, *Proc. SPIE*, **10698**, 106981X
 Gaskell, R., Barnouin-Jha, O. S., Scheeres, D., et al. 2006, in *AIAA/AAS Astrodynamics Specialist Conf. and Exhibit* (Reston, VA: AIAA), 2006-6660, doi:10.2514/6.2006-6660
 Gaskell, R. W. 2012, *AAS/DPS Meeting*, **44**, 209.03
 Gaskell, R. W., Barnouin-Jha, O. S., Scheeres, D., et al. 2008, *M&PS*, **43**, 1049
 Gaskell, R. W., Synnott, S. P., McEwen, A. S., & Schaber, G. G. 1988, *GeoRL*, **15**, 581
 Gault, D. E., & Wedekind, J. A. 1978, *LPSC*, **9**, 3843
 Gehrels, T., Matthews, M. S., & Schumann, A. M. 1994, *Hazards Due to Comets and Asteroids*, Space Science Series (Tucson, AZ: Univ. Arizona Press)
 Holsapple, K. A., & Housen, K. R. 2012, *Icar*, **221**, 875
 Ieva, S., Mazzotta Epifani, E., Perna, D., et al. 2022, *PSJ*, **3**, 183
 Jorda, L., Gaskell, R., Capanna, C., et al. 2016, *Icar*, **277**, 257
 Jorda, L., Lamy, P. L., Gaskell, R. W., et al. 2012, *Icar*, **221**, 1089
 Jutzi, M., & Michel, P. 2014, *Icar*, **229**, 247
 Kitazato, K., Clark, B. E., Abe, M., et al. 2008, *Icar*, **194**, 137
 Larson, J. N., & Sarid, G. 2021, *MNRAS*, **503**, 1070
 Lowry, S. C., Weissman, P. R., Hicks, M. D., Whiteley, R. J., & Larson, S. 2005, *Icar*, **176**, 408
 Magrin, S., La Forgia, F., Pajola, M., et al. 2012, *P&SS*, **66**, 43
 Mario, C. E., Miller, C. J., Norman, C. D., et al. 2022, *PSJ*, **3**, 104
 McEwen, A. S. 1996, *LPSC*, **27**, 841
 Michel, P., Cheng, A., Küppers, M., et al. 2016, *AdSpR*, **57**, 2529
 Michel, P., Küppers, M., Campo Bagatin, A., et al. 2022, *PSJ*, **3**, 160
 Murchie, S., Robinson, M., Clark, B. E., et al. 2002, *Icar*, **155**, 145
 Naidu, S. P., Benner, L. A. M., Brozovic, M., et al. 2020, *Icar*, **348**, 113777
 Naidu, S. P., Chesley, S. R., & Farnocchia, D. 2021, *Jet Propulsion Laboratory Interoffice Memorandum*, 392R-21-004
 Nolan, M. C., Magri, C., Howell, E. S., et al. 2013, *Icar*, **226**, 629
 Olds, R., Miller, C. J., Norman, C. D., et al. 2022, *PSJ*, **3**, 100
 Pajola, M., Barnouin, O. S., Lucchetti, A., et al. 2022, *PSJ*, submitted
 Palmer, E., Gaskell, R., Daly, M., et al. 2022, *PSJ*, **3**, 102
 Park, R. S., Vaughan, A. T., Konopliv, A. S., et al. 2019, *Icar*, **319**, 812
 Perna, D., Barucci, M. A., & Fulchignoni, M. 2013, *A&ARv*, **21**, 65
 Perry, M. E., Neumann, G. A., Phillips, R. J., et al. 2015, *GeoRL*, **42**, 6951
 Pravec, P., Harris, A. W., Kušnirák, P., Galád, A., & Hornoch, K. 2012, *Icar*, **221**, 365
 Pravec, P., Scheirich, P., Kušnirák, P., et al. 2006, *Icar*, **181**, 63
 Pravec, P., Scheirich, P., Kušnirák, P., et al. 2016, *Icar*, **267**, 267
 Pravec, P., Thomas, C. A., Rivkin, A. S., et al. 2022, *PSJ*, **3**, 175
 Raducan, S. D., Davison, T. M., & Collins, G. S. 2022, *Icar*, **374**, 114793
 Re, C., Fennema, A., Simioni, E., et al. 2022, *P&SS*, submitted
 Richardson, D. C., Agrusa, H. F., Barbee, B., et al. 2022, *PSJ*, **3**, 157
 Rivkin, A. S., Chabot, N. L., Stickle, A. M., et al. 2021, *PSJ*, **2**, 173
 Scheeres, D. J., McMahan, J. W., Jones, B. A., & Doostan, A. 2015, *IEEE Aerospace Conf. (Piscataway, NJ: IEEE)*, 1
 Scheirich, P., & Pravec, P. 2022, *PSJ*, **3**, 163
 Schwartz, S. R., Yu, Y., Michel, P., & Jutzi, M. 2016, *AdSpR*, **57**, 1832
 Sierks, H., Lamy, P., Barbieri, C., et al. 2011, *Sci*, **334**, 487
 Simioni, E., Re, C., Mudric, T., et al. 2021, *P&SS*, **198**, 105165
 Stickle, A. M., Atchison, J. A., Barnouin, O. S., et al. 2015, *Procedia Engineering*, **103**, 577
 Stickle, A. M., Burger, C., Caldwell, W. K., et al. 2022, *PSJ*, submitted
 Sval, M. B., Owen, J. M., & Miller, P. L. 2016, *Icar*, **269**, 50
 Tanbakouei, S., Trigo-Rodríguez, J. M., Sort, J., et al. 2019, *A&A*, **669**, A119
 Tatsumi, E., Sugimoto, C., Riu, L., et al. 2021, *NatAs*, **5**, 39
 Thomas, N., Cremonese, G., Zethé, R., et al. 2017, *SSRv*, **212**, 1897
 Watanabe, S., Hirabayashi, M., Hirata, N., et al. 2019, *Sci*, **364**, 268
 Weirich, J., Palmer, E. E., Daly, M. G., et al. 2022, *PSJ*, **3**, 103
 Wolf, P. R., & Dewitt, B. A. 2000, *Elements of Photogrammetry with Applications in GIS* (Boston, MA: McGraw-Hill)
 Yu, Y., Michel, P., Schwartz, S. R., Naidu, S. P., & Benner, L. A. M. 2017, *Icar*, **282**, 313